JAMES | Journal of Advances in Modeling Earth Systems®

RESEARCH ARTICLE
10.1029/2024MS004567

Internal Ocean-Atmosphere Variability in Kilometer-Scale Radiative-Convective Equilibrium

Adam B. Sokol[1,2], Vlad A. Munteanu[2], Peter N. Blossey[2], and Dennis L. Hartmann[2]

[1]Program in Atmospheric and Oceanic Sciences, Princeton University, Princeton, NJ, USA, [2]Department of Atmospheric and Climate Science, University of Washington, Seattle, WA, USA

Key Points:

- Coupled, cloud-resolving radiative-convective equilibrium supports coherent, internal oscillations in mean sea surface temperature (SST), spatial SST contrast, and convective organization
- When convection is more organized, the overturning circulation is slower and more bottom-heavy
- The static stability of the upper troposphere is modulated by SST, while that at lower levels is modulated by convective organization

Supporting Information:

Supporting Information may be found in the online version of this article.

Correspondence to:

A. B. Sokol,
adam.sokol@princeton.edu

Citation:

Sokol, A. B., Munteanu, V. A., Blossey, P. N., & Hartmann, D. L. (2025). Internal ocean-atmosphere variability in kilometer-scale radiative-convective equilibrium. *Journal of Advances in Modeling Earth Systems*, *17*, e2024MS004567. https://doi.org/10.1029/2024MS004567

Received 18 JUL 2024
Accepted 9 MAY 2025

Author Contributions:

Conceptualization: Adam B. Sokol, Dennis L. Hartmann
Data curation: Adam B. Sokol
Formal analysis: Adam B. Sokol, Vlad A. Munteanu
Funding acquisition: Adam B. Sokol, Dennis L. Hartmann
Methodology: Adam B. Sokol
Project administration: Dennis L. Hartmann

Abstract We describe internal, low-frequency variability in a 21-year simulation with a cloud-resolving model. The model domain is the length of the equatorial Pacific and includes a slab ocean, which permits coherent cycles of sea surface temperature (SST), atmospheric convection, and the convectively coupled circulation. The warming phase of the cycle is associated with near-uniform SST, less organized convection, and sparse low cloud cover, while the cooling phase exhibits strong SST gradients, highly organized convection, and enhanced low cloudiness. Both phases are quasi-stable but, on long timescales, are ultimately susceptible to instabilities resulting in rapid phase transitions. The internal cycle is leveraged to understand the factors controlling the strength and structure of the tropical overturning circulation and the stratification of the tropical troposphere. The overturning circulation is strongly modulated by convective organization, with SST playing a lesser role. When convection is highly organized, the circulation is weaker and more bottom-heavy. Alternatively, tropospheric stratification depends on both convective organization and SST, depending on the vertical level. SST-driven variability dominates aloft while organization-driven variability dominates at lower levels. A similar pattern is found in ERA5 reanalysis of the equatorial Pacific. The relationship between convective organization and stratification is explicated using a simple entraining plume model. The results highlight the importance of convective organization for tropical variability and lay a foundation for future work using coupled, idealized models that explicitly resolve convection.

Plain Language Summary Interactions between ocean temperature patterns and deep convection in the tropics play an important role in climate variability and change. To study these interactions, we run an idealized, high-resolution model of the tropical atmosphere over an interactive ocean surface for 21 years. To our knowledge, this is the first time a coupled, high-resolution model has been run for so long, allowing us to examine the variability that develops on long timescales. The conditions we impose on the model are completely uniform in space and time, but the simulation nevertheless produces large cycles of internally generated climate variability. In the cycle, the mean ocean temperature, the spatial pattern of ocean temperature (uniform vs. nonuniform), and the large-scale organization of deep convection all vary together in a systematic way. In one phase of the cycle, the climate gradually warms, the ocean temperature is relatively uniform across the model domain, and there are two regions of deep convection. In the other phase, there are strong temperature gradients, convection is confined to a single region, and the mean climate gradually cools. We exploit this cycle of variability to study several questions about the structure of the tropical atmosphere and tropical circulations.

1. Introduction

The spatial distribution of sea surface temperature (SST) in the tropical Pacific plays a critical role in the internal variability of Earth's climate as well as its response to forcing (Andrews et al., 2018; Bjerknes, 1969). The tropical SST pattern is set not only by ocean dynamics, but also by interactions between tropical convection, clouds, and the large-scale atmospheric circulation (Deser et al., 2010; Knutson & Manabe, 1995; Ramanathan & Collins, 1991; Vecchi & Soden, 2007). Understanding these interactions and their role in internal climate variability is critical for making sense of future climate projections (Wills et al., 2022). Our primary focus here is on the atmospheric component of that variability, which we explore using a model in which ocean dynamics are neglected but the SST is responsive to atmospheric processes.

The upward transport of mass by deep convection is an important factor in tropical climate variability. The strength and organization of convective mass flux affects large-scale overturning circulations such as the east-west Walker circulation in the equatorial Pacific. Walker circulation strength can, in turn, impact the spatial

Software: Adam B. Sokol, Peter N. Blossey
Supervision: Dennis L. Hartmann
Visualization: Adam B. Sokol
Writing – original draft: Adam B. Sokol
Writing – review & editing: Adam B. Sokol, Vlad A. Munteanu, Peter N. Blossey, Dennis L. Hartmann

pattern of SST (Bjerknes, 1969; Vecchi & Soden, 2007), which feeds back on the large-scale organization of convection. Even in the absence of SST feedbacks, the organization of convection may affect the convective mass flux and large-scale circulation via its impact on the structure of the tropical troposphere. Convective organization is known to affect the dry static stability of the troposphere (Becker et al., 2018; Bony et al., 2016), which in models has important implications for overturning circulation strength (Knutson & Manabe, 1995; Ma et al., 2012; Sohn et al., 2016). Organization also impacts the area covered by convectively generated anvil clouds, which themselves affect the large-scale circulation via cloud radiative heating (Voigt et al., 2019). In fully coupled general circulation models (GCMs) with parameterized convection and realistic boundary conditions, it can be difficult to disentangle the various mechanisms by which SST, convection, and circulation interact. Idealized modeling experiments, such as the radiative-convective equilibrium simulations presented here, are useful for understanding the fundamental processes at play.

Radiative-convective equilibrium (RCE) is one of the simplest models of Earth's atmosphere. It describes the statistical equilibrium between radiative cooling and convective heating and is a good approximation of the tropical atmosphere at large spatiotemporal scales (Jakob et al., 2019). RCE models of varying complexity have long been used as a test bed for understanding many atmospheric and climatic phenomena, such as the influence of CO_2 on surface temperature (e.g., Manabe & Wetherald, 1967), the effect of climate change on precipitation (e.g., Romps, 2011), and even the effects of nuclear winter on the thermal structure of the atmosphere (Ramaswamy & Kiehl, 1985). More pertinently to this work, RCE has been used extensively to understand the SST dependence of convective cloud properties (e.g., Harrop & Hartmann, 2012; Seeley et al., 2019; Seidel & Yang, 2022), convective organization (e.g., Bretherton et al., 2005; Cronin & Wing, 2017; Wing et al., 2017), and the tropical overturning circulation (e.g., Jeevanjee, 2022; Jenney et al., 2020). These studies have typically simulated RCE using limited-area, convection-resolving models with a lower boundary that is spatially and temporally uniform.

Several studies have explored the mean state and internal variability of RCE models coupled to an interactive ocean. These experiments have typically used GCMs with parameterized convection and a simple mixed-layer ("slab") ocean, in which dynamic transport is neglected and the SST evolves according to the local energy imbalance at the surface. They have typically adopted some variation of a "Tropic World" protocol (Hartmann & Dygert, 2022), in which the Earth is a nonrotating, spherical aquaplanet with horizontally uniform insolation. In the first of such experiments, Popke et al. (2013) found that convection organized into features of various size and that the SST varied by 6–9 K across the globe, depending on the convection scheme. Reed et al. (2015) found that slab ocean simulations were associated with a reduced degree of convective organization compared to fixed-SST runs, although both configurations exhibited clearly defined regions of convection and large-scale subsidence. In their simulations, the global mean SST was relatively steady after the initial equilibration period. In contrast, experiments by Coppin and Bony (2017) featured oscillations in global mean SST, spatial SST contrast, convective organization, and low cloudiness with a timescale dependent on slab ocean depth. Mean SST and convective organization were out-of-phase with one another, with periods of enhanced SST contrast were associated with global mean cooling. Drotos et al. (2020) performed experiments with varying CO_2 levels and found irregular oscillations in global mean SST of ∼8 K. The cycles were driven by variability in inversion strength at the top of the planetary boundary layer (PBL), which drove the rather abrupt formation and collapse of low, stratiform cloud decks. Notably, this large-amplitude variability only occurred for CO_2 concentrations of at least 8 times the preindustrial reference of 278 ppm. Dygert and Hartmann (2023) described a unique mode of variability in which the SST contrast varied substantially but the mean SST was relatively steady. In those cycles, SST contrast developed due to spatial contrasts in low cloud cover, surface evaporation, and free tropospheric humidity and collapsed due to down-gradient energy transport by the atmospheric circulation, among other factors. All of these studies used GCMs with parameterized convection.

In this work, we examine internal variability in coupled RCE simulations using a cloud-resolving model (CRM) that explicitly resolves convection. CRMs are widely used to investigate tropical cloud and convective processes but, in contrast to the GCM studies described above, are most often run for short integration times on limited-area, doubly periodic domains with fixed SSTs (e.g., Wing et al., 2018). Simple slab oceans have been used in a handful of experiments (Bretherton et al., 2005; Y.-T. Chen & Wu, 2019; Hohenegger & Stevens, 2016; Shamekh et al., 2020; Tompkins & Semie, 2021), most of which investigated the impact of interactive SSTs on the initial onset of convective aggregation. Here, we focus on much longer timescales by integrating a CRM for over 21 years on a domain that is as long as the equatorial Pacific basin. On these timescales, the coupled system

develops an internal cycle in which SST (both its mean value and its spatial distribution), convective organization, and the atmospheric circulation vary coherently.

We begin by describing the simulation (Section 2) and the cycles of coupled variability that it produces (Section 3). We then take a closer look at variability in convective mass flux and the large-scale circulation (Section 4). In Section 5, we leverage the internal cycles and a simple entraining plume model to investigate the stratification of the tropical troposphere. Section 6 provides a discussion and conclusions.

2. Data and Methods

2.1. Model Simulations

We use the System for Atmospheric Modeling v6.10 (SAM; Khairoutdinov & Randall, 2003) with the P3 microphysics scheme (Morrison et al., 2015). The model domain is two-dimensional, has 3-km horizontal resolution, and has a length of 13,122 km—similar to the size the tropical Pacific basin. The variable-resolution vertical grid has 81 levels with a spacing of 80 m near the surface, 333 m throughout most of the troposphere, and ∼1 km near the model top at 29.4 km. The mean horizontal wind is nudged to zero on a one-day timescale to avoid oscillations in the mean wind that are known to develop in two-dimensional RCE (Held et al., 1993). The simulation uses a fifth-order advection scheme (Yamaguchi et al., 2011) and SAM's original 1.5-order subgrid-scale closure.

The atmosphere is coupled to a 25-m slab ocean. At each model time step, the SST at each grid point evolves in response to local energy fluxes at the surface:

$$\rho_w C_w H \frac{d}{dt} SST(x,t) = SW(x,t) + LW(x,t) + LHF(x,t) + SHF(x,t) - Q \quad (1)$$

here, ρ_w and C_w are the density and specific heat capacity of water, and $H = 25\text{m}$ is the ocean depth. SW and LW are the net downward shortwave and longwave fluxes at the surface, respectively. LHF and SHF are the latent and sensible heat fluxes, respectively, defined as positive downward. Q is the parameterized ocean heat sink (hereafter the Q-flux), which is applied uniformly in space and time. The Q-flux is intended to mimic the export of heat from the tropics to the midlatitudes, and it is necessary for achieving reasonable SSTs under realistic tropical insolation, which in these experiments follows a diurnal cycle with a mean of 413.8 W/m^2. This simulation uses $Q = 35$ W/m^2, which was found by trial and error to produce SSTs similar to those in the present-day equatorial Pacific.

To speed up the initial ocean adjustment process, we first integrated a run with $H = 10$ m for 100 days. This run is initialized with a uniform SST of 302 K. We then switched to $H = 25$ m and began the main run examined in this paper, which was integrated for 7,900 days (>21 years). Unless stated otherwise, results reflect the last 4,900 days of the simulation, over which the mean is 301.2 K. Results requiring vertically resolved output rely on the last 400 days, when full output was collected every 2 hours.

We have chosen to use a 2D model domain due to computational considerations and our interest in low-frequency variability. Previous work has documented several systematic differences between 2D and 3D CRM simulations (Grabowski et al., 1998; Petch et al., 2008; Tompkins, 2000), but these differences are primarily relevant on short timescales and for flows with highly three-dimensional structure. Because we are interested in the low-frequency variability of Walker-type circulations (which have highly two-dimensional geometry), we anticipate that processes critical for our results are faithfully represented in two dimensions. Nevertheless, it is possible that certain biases introduced by 2D domains, such as the tendency to produce strong low-level winds, could systematically impact the SST evolution in this simulation.

2.2. Analysis Tools and Metrics

We use several metrics to quantify various aspects of the SST field throughout the simulation. We first define the domain-averaged SST as $\overline{SST}$. However, according to conceptual models of the tropical atmosphere, the mean SST is not necessarily the best indicator of the thermodynamic state of the free troposphere. In the tropics, horizontal buoyancy anomalies are efficiently homogenized by gravity waves, which constrains free-tropospheric temperatures in nonconvecting regions to be roughly equal to those in convective regions (Bretherton & Smolarkiewicz, 1989). Within the convective region, rising updrafts roughly follow a moist adiabatic temperature

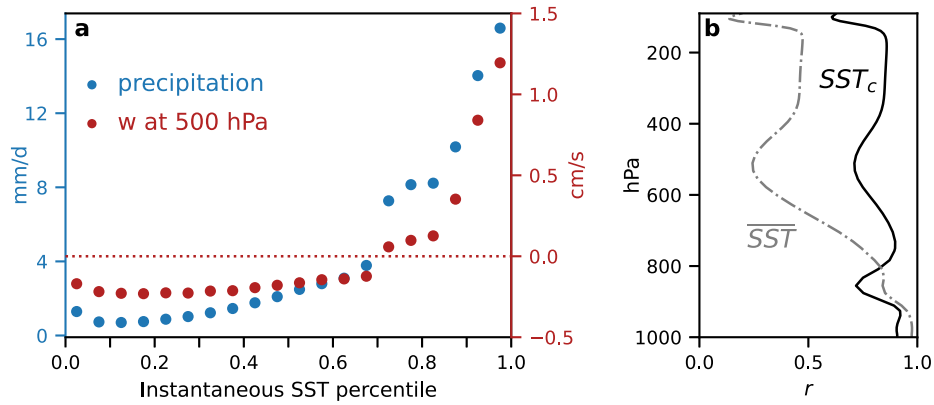

Figure 1. (a) Mean precipitation and 500-hPa vertical velocity sorted by sea surface temperature (SST) percentile. SST percentiles are computed for each day of the simulation such that 0 and 1 represents the coldest and warmest SSTs on any given day, regardless of the domain-averaged SST. Bin widths: 0.05. (b) Correlation coefficients between the daily mean temperature at each model level and (black) SST_c and (dashed gray) $\overline{SST}$.

profile corresponding to the sub-cloud entropy, which is closely tied to the underlying SST (Emanuel et al., 1994). We may therefore expect the thermodynamic variability of the free troposphere to be more directly tied to the SST in actively convecting regions than to $\overline{SST}$. For this reason, we define SST_c as the mean SST in the warmest 30% of the model domain, which we take to represent regions of active convection. The 30% threshold has been used in previous work (Fueglistaler, 2019) and is suitable here as well, judging by the SST percentile-sorted precipitation rate and 500-hPa vertical velocity shown in Figure 1a. The warmest 30% of the domain accounts for 73% of the total precipitation and undergoes mean ascent at 500 hPa, compared to mean subsidence elsewhere. Indeed, Figure 1b shows that SST_c is significantly more predictive of domain-averaged, free tropospheric temperature than $\overline{SST}$. We thus adopt SST_c in lieu of $\overline{SST}$ for many parts of our analysis.

We quantify the degree of spatial SST contrast as the standard deviation of SST across the domain, denoted as σ_{SST}. To understand the drivers of SST contrast, we compute the budget for σ^2_{SST}, the spatial variance of SST. Following Tompkins and Semie (2021) and Hartmann and Dygert (2022), the prognostic equation for σ^2_{SST} is

$$\frac{d}{dt}\sigma^2_{SST} = \left(\rho_w C_w H\right)^{-1}\left(\overline{SST'SW'} + \overline{SST'LW'} + \overline{SST'LHF'} + \overline{SST'SHF'}\right) \quad (2)$$

where bars denote the domain average and primes the deviation from that average. The four terms on the RHS are computed from instantaneous 2-D output, which is collected every 2 hr throughout the simulation. The Q-flux term is not present in Equation 2 because it is spatially uniform and thus does not contribute to SST variance.

2.3. Reanalysis

As a point of comparison throughout the paper, we use the ERA5 reanalysis produced by the European Centre for Medium-Range Weather Forecasts (Hersbach et al., 2020). Monthly mean temperature, specific humidity, and SST were retrieved at a horizontal resolution of 0.25° × 0.25° for the 1990–2023 period. The study region is the equatorial Pacific (15°S–15°N, 140°E–260°E), which was selected such that its zonal extent is approximately equal to the length of the model domain. The 1990–2023 mean SST for the region is 301.0 K, only 0.2 K cooler than the model simulation.

In Section 5, we make use of the column relative humidity (RH) $\mathcal{H}$ = CWV/CWV*, where CWV is the column-integrated water vapor and CWV* is the CWV at saturation. In the reanalysis, we compute $\mathcal{H}$ using the monthly mean temperature and specific humidity data at each grid cell. The calculation uses a linear transition from ice to liquid saturation between 253.15 and 273.15 K.

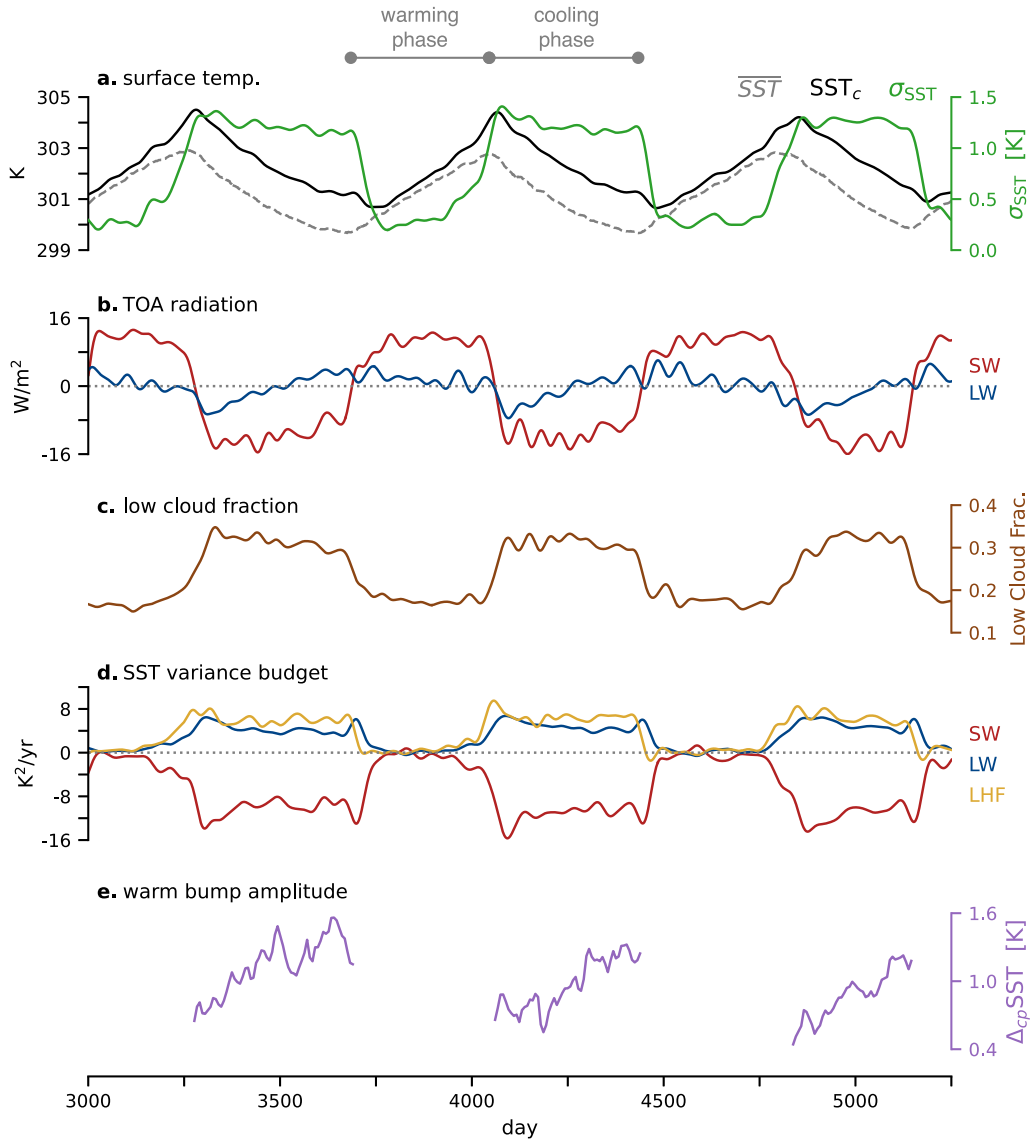

Figure 2. Time series of various quantities for a 2,250-day period of the simulation. (a) Various sea surface temperature (SST) metrics; (b) net top-of-atmosphere downward radiation; (c) low cloud fraction; (d) the three leading terms of SST variance budget; (e) $\Delta_{cp}SST$, the metric developed in Section 3.1 that quantifies the SST difference between the warmest and coldest parts of the cold, nonconvective region. For clarity, all time series except $\overline{SST}$ and $\Delta_{cp}SST$ are low-pass filtered using a 4th-order Butterworth filter with a 50-day cutoff.

3. Description of the Cycle of Internal Variability

Figure 2 provides an overview of the cycle and time series of its important components. The cycle can also be represented within a phase space defined by $\overline{SST}$ and σ_{SST}, shown in Figure 3. The phase diagram summarizes various aspects of the cycle that will be further developed in the following sections.

The cycle is defined by two phases, which are seen clearly in Figures 2a and 3: A cooling phase, in which σ_{SST} is high and $\overline{SST}$ steadily declines, and a warming phase, in which SSTs are relatively uniform and $\overline{SST}$ increases. In other words, more uniform SSTs are associated with mean warming and spatially varying SSTs with mean cooling. σ_{SST} hovers around 0.3 and 1.2 K, respectively, during the warming and cooling phases of the cycle. The latter is similar to the typical standard deviation of SST across the equatorial Pacific study region (0.93 K). The boxcar-like variability of σ_{SST} (Figure 2a) indicates that the transitions between the two phases are fast relative to the timescale of the full cycle.

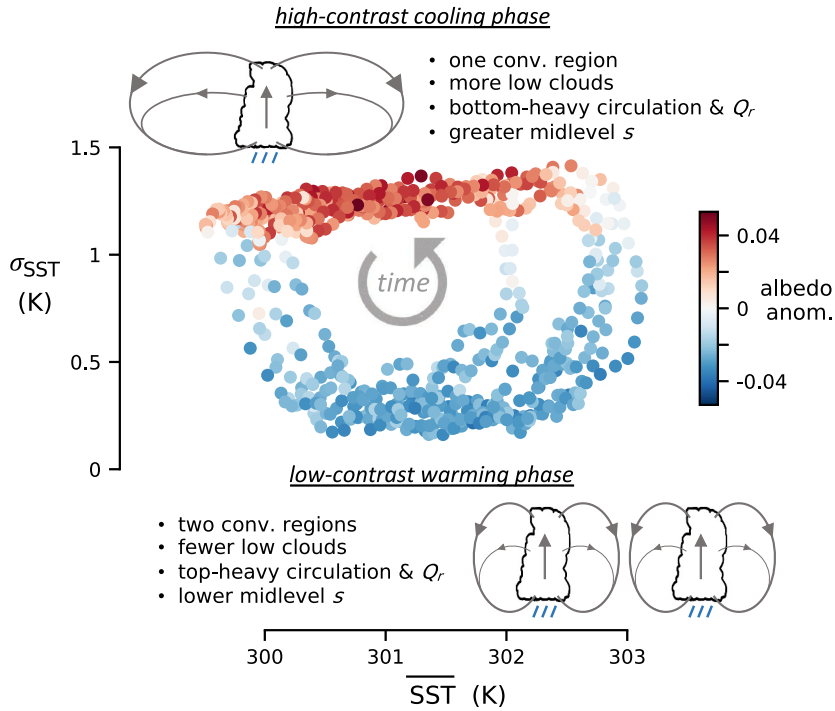

Figure 3. Phase diagram of the cycle in $\overline{SST}$-σ_{SST} phase space. Each scatter point represents a 7-day period and is shaded according to the domain-averaged albedo anomaly. The circular arrow represents the direction in which the cycle progresses over time.

Over the 4,900-day simulation period used for results, there are seven full iterations of the cycle. While the σ_{SST} cycle amplitude is relatively consistent throughout the simulation (Figure 3), the $\overline{SST}$ cycle amplitude varies from 2.0 to 3.6 K with an average of 2.8 K. This is a greater range of $\overline{SST}$ variability than that found in the equatorial Pacific study region (Section 2.3), where the monthly mean, area-averaged SST varies by ∼1 K in a typical year and by 2.1 K over the entire 34-year study period. These values, however, are quite sensitive to the study region boundaries. For example, the monthly mean SST along the equator between 140° and 260°E varies by ∼2 K in a typical year and by 4.6 K over the entire study period. The range of $\overline{SST}$ variability in the simulation therefore seems on par with SST variability in the equatorial Pacific. Notably, the iteration immediately preceding the 4,900-day results period had an anomalously large amplitude of 4.6 K (Figure S1 in Supporting Information S1). This iteration was typical in all other respects, but we exclude it from the results period due to its outsized statistical influence. Possible explanations for the large-amplitude iteration are discussed in Section 3.2.

The $\overline{SST}$ cycle is driven by variability in absorbed SW radiation. Figure 2b shows that, like σ_{SST}, top-of-atmosphere (TOA) SW anomalies exhibit boxcar-like variability, with a difference of about 25–30 W/m^2 between the warming and cooling phases of the cycle. The difference in absorbed SW is caused by changes in low cloud area, which is about a factor of two greater during the cooling phase (Figure 2c). Compared to SW, the role of TOA LW flux variability in the $\overline{SST}$ cycle is minor. The domain-average LW flux varies by ∼10 W/m^2 throughout the cycle but does not differ systematically between the warming and cooling phases. Rather, the temporal variability of the LW flux is dominated by the Planck response to changes in SST_c.

Throughout the cycle, spatial contrasts in SST are associated with similar contrasts in deep convective activity and precipitation (Figure 4). It is important to distinguish here between convective *aggregation*—which describes the tendency of convection to cluster into well defined regions in numerical simulations (Wing et al., 2017)—and convective *organization*, which refers to broader, non-specific ways in which convection clusters in space and time (Pendergrass, 2020). Figure 4b shows that convection remains aggregated throughout the entire cycle, that is, there are always well defined regions of moisture and precipitation within the otherwise dry domain. On the other hand, the large-scale organization of convection varies systematically throughout the cycle. During the high-σ_{SST} phase, deep convection and heavy precipitation are confined to a single region over the warm pool, and low cloud

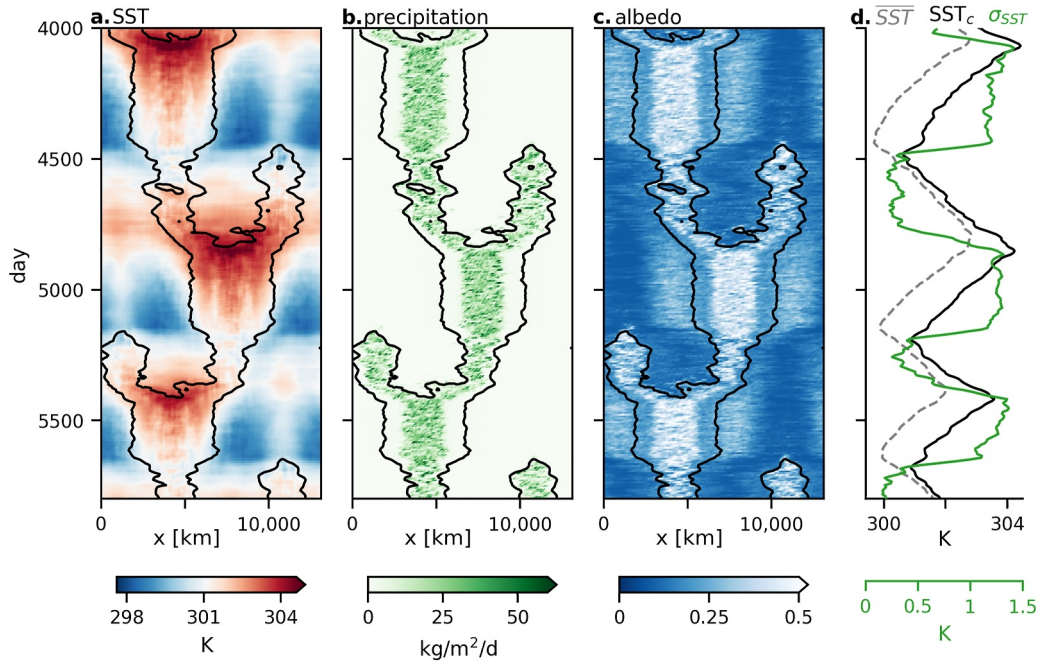

Figure 4. Hovmöller diagrams of weekly mean (a) sea surface temperature, (b) precipitation, and (c) albedo for a 1,800-day period of the simulation. Data are coarsened to a horizontal resolution of 81 km for plotting. The black contour indicates a column relative humidity of 0.6 and is intended to loosely enclose regions of active convection. (d) Time series of $\overline{SST}$, SST_c, and σ_{SST} reproduced from Figure 2a.

regions are found over the cooler SSTs on both sides of the convective region. During the low-σ_{SST} phase, there are two convective regions and low clouds are less abundant. The relationship between σ_{SST} and the number of large-scale convective regions (one or two) is one-to-one throughout the cycle (Figure S2 in Supporting Information S1), which allows σ_{SST} to be used as a proxy for large-scale convective organization going forward.

The period of the cycle, which we expect to be dependent on H (Coppin & Bony, 2017), is 680 days on average but ranges from 500 to 900 days. We conducted a sensitivity test to confirm that a change in H would not fundamentally alter the characteristics of the cycle. For this test, we restart the simulation from its end (day 7,900) and integrate the model for an additional 800 days with $H = 5$ m. Consistent with Coppin and Bony (2017), we find that decreasing H results in a faster and noisier internal cycle but that the basic characteristics of the variability are unchanged (Figure S3 in Supporting Information S1).

The remainder of this section examines the cooling and warming phases of the cycle in greater detail, then discusses similarities to previous work. The cooling phase is also referred to as the "high-contrast" or "high-σ_{SST}" phase, while the warming phase is also referred to as the "low contrast" or "low-σ_{SST}" phase.

3.1. High-Contrast Cooling Phase

The cooling phase of the cycle is broadly analogous to the equatorial Pacific during La Niña conditions, when there is a strong zonal SST gradient and Walker circulation. The model domain features distinct warm and cold regions, with a difference of ~3–3.5 K between the minimum and maximum SSTs (Figure 5e). Deep convection, precipitation, and large-scale ascent are confined to a single region over the warmest SSTs, while cooler SSTs and large-scale subsidence occupy the rest of the domain (Figures 5a, 5c, and 5e).

The SST variance budget, given by Equation 2 and shown in Figure 2d, shows that spatial contrasts in SST are maintained by the LW and LHF terms of the budget and damped by the SW term. In the warm region, longwave cooling of the surface is ineffective due to a stronger greenhouse effect there, and latent heat fluxes are weak due to high near-surface humidity and relatively weak surface winds (Figure 5e, Figure S4 in Supporting Information S1). Because surface evaporation is weak in the warm pool, the strong water vapor greenhouse there is supported by the import of moisture by the atmospheric circulation (not shown). In the cold region, the surface

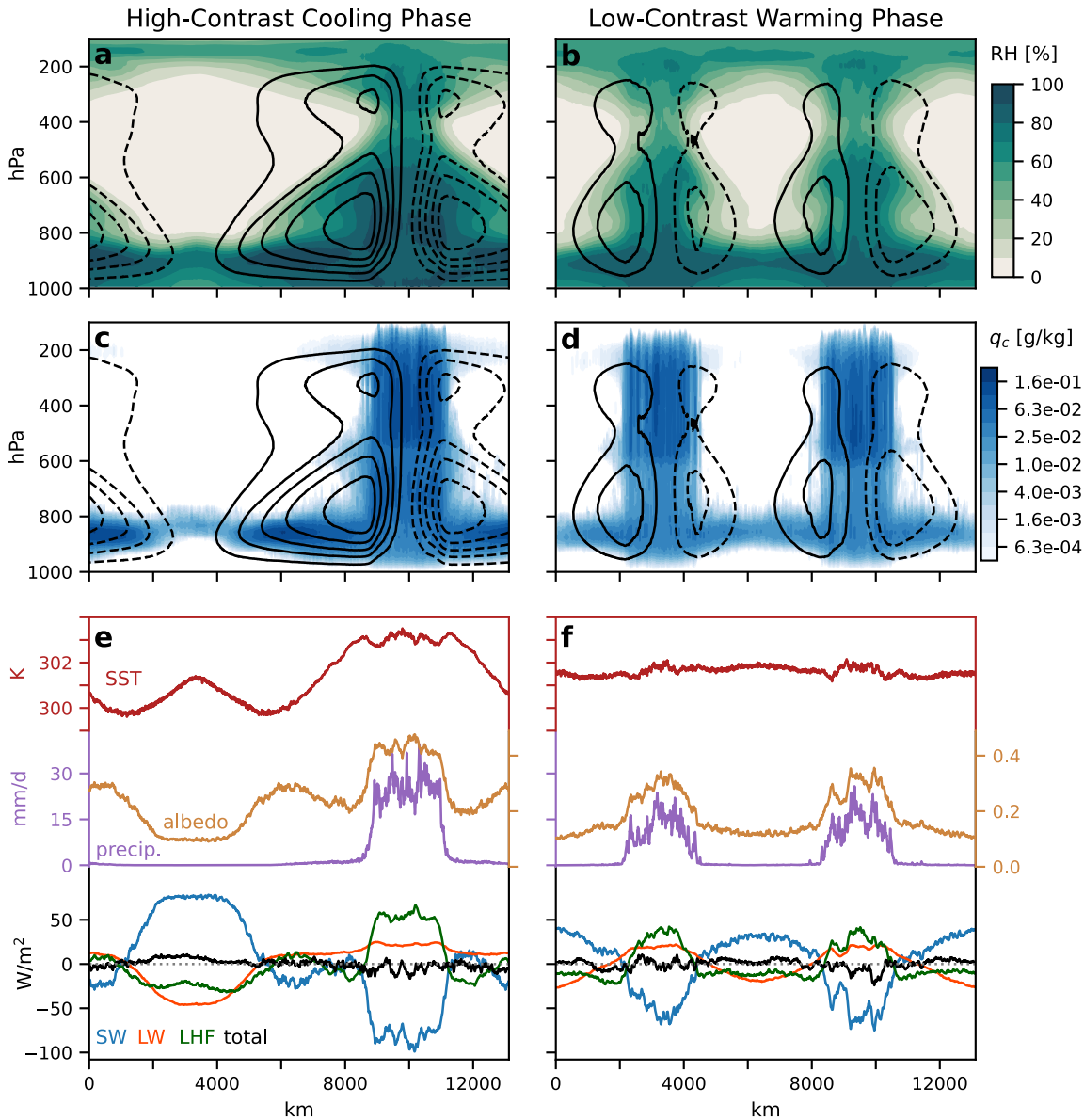

Figure 5. Characteristics of the (a, c, e) high-contrast cooling phase and (b, d, f) low-contrast warming phase. (a), (b) Relative humidity. (c), (d) Total nonprecipitating cloud condensate. Contours in panels (a)–(d) show the mass streamfunction with an interval of 4,000 kg m^{-1} s^{-1} (solid are positive; dashed are negative; zero contour not shown). (e), (f) sea surface temperature, albedo, precipitation, and the surface energy budget. Energy budget terms are expressed as anomalous fluxes with respect to the domain average, with positive values indicating anomalous downward flux into the surface (i.e., a surface warming tendency). The sum of the individual terms (black line) includes the small sensible heat flux term. All data reflect the average of 2-hourly instantaneous output over 50-day periods within each phase of the cycle. The energy budget terms are smoothed with a 39-km running mean for clarity.

cools more effectively by LW emission due to the dryness of the free troposphere above, especially in the center of the subsiding region. In addition, strong surface winds and/or reduced near-surface humidity generate enhanced latent heat fluxes that cool the surface. Shortwave fluxes act to reduce σ_{SST} at all times, since deep convective clouds shade the warmest SSTs.

Within the cool, nonconvective region of the domain, SST is far from uniform (Figures 4a and 5e). The coldest SSTs are found at the edges of the cold region, whereas the center of cold region is ∼1 K warmer than the edges (albeit still colder than the warmer convecting region; Figure 5e). This "cold edge-warm center" pattern is a critical component of the cycle of internal variability. A similar pattern has appeared in spherical GCM simulations (see Figure 2 in Dygert & Hartmann, 2023), suggesting that it is not an artifact of this simulation's 2-D

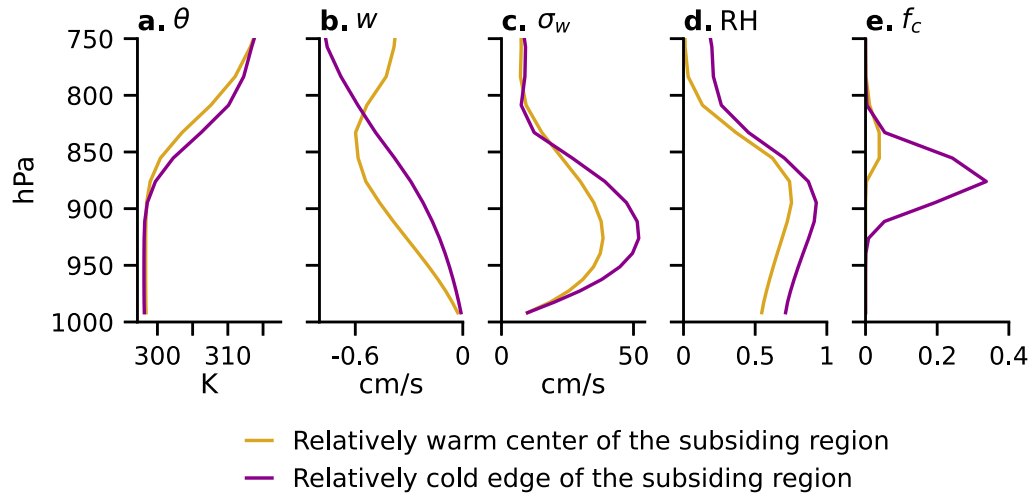

Figure 6. Profiles of panel (a) potential temperature, (b) vertical velocity, (c) the standard deviation of the vertical velocity, (d) relative humidity, and (e) cloud fraction averaged over the (gold) relatively warm, cloud-free center and (purple) the relatively cold, cloudy edges of the subsiding region. Profiles are computed from vertically resolved output over a 50-day period during the high-contrast phase (day 7,500–7,550).

geometry. Here, the pattern arises due to the contrast in SW absorption between the edges of the cold region, which are shaded by abundant low clouds, and the center, which is nearly cloud-free (Figures 4c and 5e). To understand why this pattern develops, Figure 6 shows the structure of the PBL over the center and edges of the subsiding region. In the center, the large-scale circulation drives mean subsidence that extends deep into the PBL, drying it out (Figure 6b). As the lower branch of the circulation accelerates from the center of the cool region toward the convective region, the PBL becomes more turbulent and is gradually moistened, as shown by the difference in RH and the standard deviation of vertical velocity (σ_w) between the warm center and cold edge of the subsiding (Figures 6c and 6d). Differences in temperature and RH at the lowest model level suggest that the lifting condensation level (LCL) decreases from 1,300 m at the center of the subsiding region to ∼600 m at the edges, consistent with a marked increase in low cloudiness (6e).

Because the contrast in low cloudiness across the subsiding region is relatively steady, the amplitude of the cold edge-warm center pattern gradually grows throughout the cooling phase of the cycle. We quantify this amplitude as $\Delta_{cp}SST$, which we define as the SST difference between the warmest 25% and the coldest 50% of the subsiding region. For this calculation, we define the subsiding region as the part of the domain where the 15-day column RH is less than 0.5, which closely traces the part of the domain with SST< $\overline{SST}$. Figure 2e shows that $\Delta_{cp}SST$ increases by nearly 1 K over the course of the cooling phase.

The end of the cooling phase is marked by the appearance of a second convective cell over the relatively warm center of the subsiding region. Figure 2e shows that this generally occurs once $\Delta_{cp}SST$ has reached ∼1.4 K, although this is not an exact threshold. We hypothesize that the formation of the second convective region is driven by the SST gradients associated with the cold edge-warm center pattern, since SST patterns are known to shape the distribution of tropical PBL convergence (Back & Bretherton, 2009; Lindzen & Nigam, 1987). The importance of the cold edge-warm center pattern to this phase transition is supported by sensitivity tests with different domain sizes (not shown, but discussed in greater detail in Section 6). $\overline{SST}$ may also play an important role in the end of the cooling phase, as evidenced by the fact that the appearance of the second convective region occurs within a relatively narrow $\overline{SST}$ range (0.7 K).

The second convective region begins as an organized, shallow convective cell (Figure 7, Movie S1). Shallow circulations are known to import energy into regions of tropical ascent (Bretherton et al., 2005; Y.-C. Chen & Yu, 2021), leading to continued growth of convective instabilities. Here, the growth of the second convective region into a matured region of deep convection takes 30–50 days. As the shallow convective cell grows, it drives compensating subsidence on both of its sides (Movie S1, around day 7,085). The subsidence causes the PBL to shallow near the edges of the cold region, eroding the low cloud cover there. The reduction in low cloud area

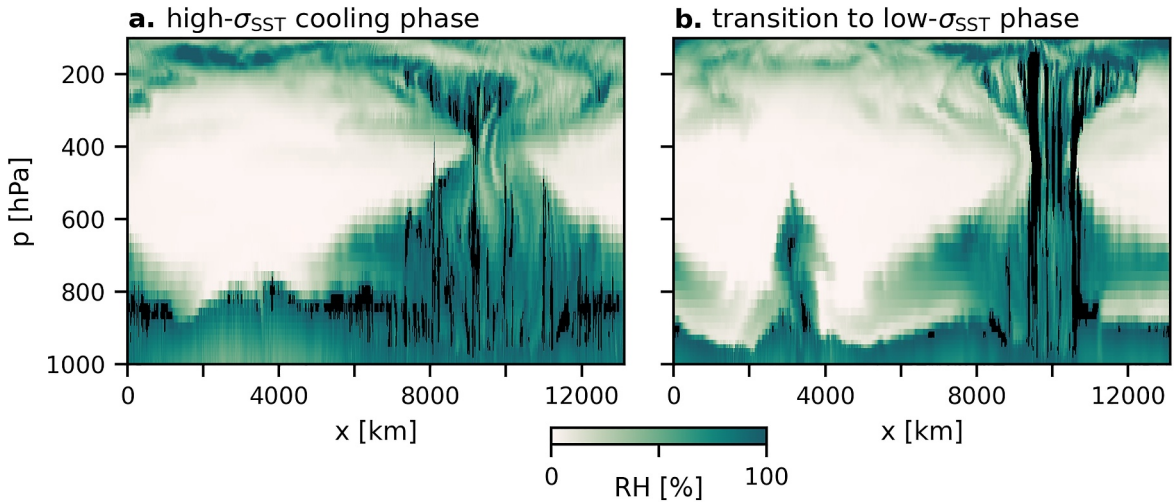

Figure 7. Snapshots of relative humidity (green shading) and clouds (black) during the (a) high-σ_{SST} cooling phase and (b) the transition from the high-σ_{SST} to low-σ_{SST} phases. In panel (b), the second convective region is seen developing over the relatively warm center of the subsiding region, and the boundary layer between the two convective regions has thinned, accompanied by a reduction in low cloud.

reduces the domain-averaged albedo, flipping the sign of the net surface energy balance and kicking off the warming phase of the cycle. By the time the warming phase begins the domain-averaged low cloud fraction has been reduced by half (Figures 2a–2c).

3.2. Low-Contrast Warming Phase

The warming phase is characterized by the relatively rapid homogenization of SSTs over ∼50 days, followed by domain-wide warming. The homogenization is achieved by warming the coldest SSTs at the edges of the subsiding region. To understand this rapid warming, we examine the SST variance budget composited around the minimum $\overline{SST}$ for seven iterations of the cycle (Figure 8a). This shows that the homogenization of SSTs begins when $\overline{SST}$ reaches its minimum value and is initially driven by the LHF term. The appearance of the second convective region interrupts the large-scale circulation, slowing the surface winds over the edges of the cold region and dampening surface evaporation (Figure S4 in Supporting Information S1). The reduction in σ_{SST} is further supported by changes in the LW term: the second convective region moistens the atmosphere over the cool SSTs, inhibiting the anomalous LW cooling there.

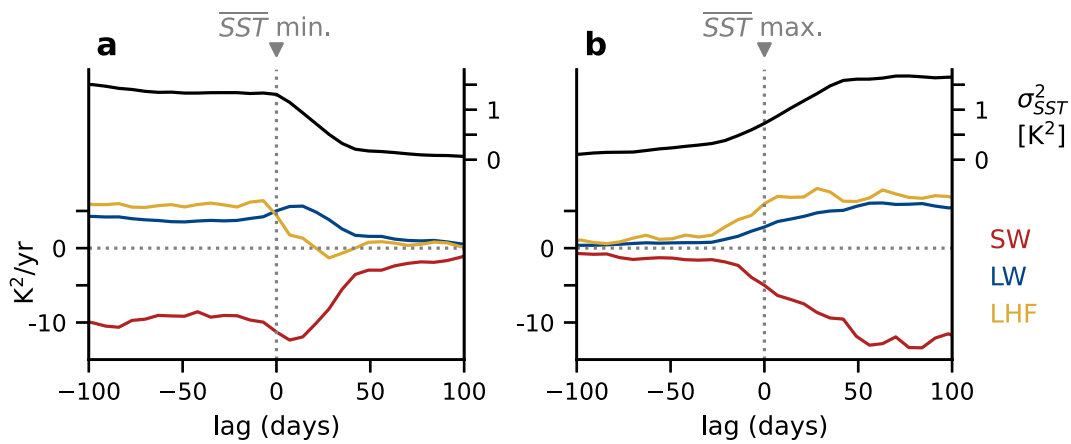

Figure 8. The three principal terms of the sea surface temperature variance budget composited around the point in the cycle where $\overline{SST}$ reaches its (a) minimum and (b) maximum; that is, $t = 0$ marks the end of the cooling phase in panel (a) and the end of the warming phase in panel (b). The black lines show the composited time series of σ^2_{SST}. The composite represents the average of seven iterations of the cycle.

Once SSTs have been homogenized, the remainder of the warming phase is characterized by the presence of two distinct convective regions and domain-wide warming. As in the cooling phase, the convective regions are flanked by areas low cloudiness on both sides, but these areas are small and the cloud cover within them is low compared to the cooling phase. As a result, the mean low cloud fraction is smaller, albedo is lower, and the domain warms. The reduced low cloudiness relative to the cooling phase is associated with drier conditions within the PBL (Figures 5a and 5b). The reduction in PBL moisture is consistent with the expected influence of the large-scale circulation on PBL moistening. During the warming phase, the large scale circulation is split into two overturning cells that are weaker and half as wide as the single cell present during the cooling phase. Wind shear within the PBL is greatly reduced, which would be expected to hinder the turbulent moistening of the PBL. Moreover, because each overturning cell is half as wide as during the cooling phase, the fetch of the low-level flow over the sea surface is reduced by half. Both of these factors would be expected to slow the moistening of the PBL, making it a less favorable environment for low cloud formation.

The transition out of the warming phase of the cycle is more gradual than the abrupt termination of the cooling phase. At the start of the warming phase, the conditions in the two subsiding regions are similar. As time progresses, a modest SST difference typically develops between the two subsiding regions (Figure 4a), accompanied by small differences in surface pressure and the strength of the low-level flow. As a result, the subsiding region with higher surface pressure gradually expands at the expense of the other, pushing the two convective regions together in the process. In the growing subsiding region, the large-scale circulation strengthens, which keeps the free troposphere dry. In the shrinking region, the circulation slows, which allows the free troposphere to be gradually moistened as the two convective regions close in. SST contrast develops throughout this period, driven principally by stronger low-level winds and enhanced evaporative cooling of the surface in the growing subsiding region. This LHF-driven contrast starts developing about ∼30 days prior to the $\overline{SST}$ maximum (Figure 8b). The growth in contrast is aided by LW radiation as the shrinking subsiding region becomes more humid while the growing subsiding region stays dry, permitting efficient surface cooling. When the two convective regions finally join, the large-scale circulation is again comprised of a single overturning cell, and the cooling phase starts anew.

The end of the warming phase is precipitated by the initial development of a SST and surface pressure difference between the two subsiding regions. Which subsiding region develops the positive SST anomaly appears to be random, and when this occurs is subject to at least some degree of stochasticity, as evidenced by the modest variability in the maximum $\overline{SST}$ achieved during each cycle iteration. This may explain, in part, why the iteration immediately preceding the 4,900-day results period reached such warm temperatures (Figure S1 in Supporting Information S1). But, excluding that outlier, the tendency of the maximum $\overline{SST}$ to fall within a ∼1 K range suggests that there is a strong thermodynamic influence on cycle amplitude and is consistent with the idea that the susceptibility of the RCE state to random perturbations is temperature dependent (Emanuel et al., 2014). Understanding what sets the upper and lower limits of the $\overline{SST}$ cycle may be a worthwhile question for future work.

3.3. Comparison to Previous Experiments

The variability described so far is similar in some respects to previous GCM results and different in others. It is most similar to the variability described by Drotos et al. (2020), in which an irregular cycle of global mean SST is driven by low cloud variability. As in our simulation, global cooling in that cycle was associated with stronger surface temperature contrast and warming with reduced contrast (see their Figure 8). In addition, the warming phase of that cycle was associated with the appearance of a new ascending region in the middle of the previous subsiding region (their Figure S4 in Supporting Information S1). A caveat is that this cycle only occurred once the time-averaged SST reached 305.8 K and was not present in simulations with a similar time-averaged SST to ours.

In addition to Drotos et al. (2020) and the present work, Coppin and Bony (2017) also described cycles in which greater SST contrast was associated with enhanced low cloudiness, more organized convection, and global mean cooling. In some of their experiments, $\overline{SST}$ and convective organization were in phase quadrature as they are here, while in others the two were out of phase. Unlike our simulation, the cycle was characterized by the repeated propagation of convection from cooler to warmer SSTs (their Figure 2), which is quite different that the oscillation between two quasi-stable states seen here.

Finally, Dygert and Hartmann (2023) also describe a coherent cycle of SST contrast, low cloudiness, and convective organization. As in the present work, turbulent surface fluxes play a critical role in the enhancement of

SST gradients. However, that cycle did not feature the significant $\overline{SST}$ variability that is seen here and other work. While there are several possible explanations for this difference, a simple possibility is that the anomalies in low cloud radiative effect were not substantial enough to drive significant change in $\overline{SST}$.

4. Circulation Variability Throughout the Cycle

Having generally described the cycle of internal variability, we turn now to variability in the convective mass flux, M, which reflects the strength and structure of the large-scale atmospheric circulation. In simple conceptual models of the tropical atmosphere, the net detrainment from convection, $\partial_p M$, is approximately balanced by the radiatively driven divergence in clear-sky regions, D_r:

$$\partial_p M \approx D_r \tag{3}$$

M is defined as positive when the convective mass flux is upward, and

$$D_r = \partial_p \omega_r \tag{4}$$

$$\omega_r = -Q_r/s \tag{5}$$

where ω_r is the radiatively driven subsidence in clear-sky regions, Q_r is the clear-sky radiative heating rate, and s is the dry static stability. Note that Equation 3 is only an approximation since radiation is not the only source of diabatic heating in clear-sky regions evaporative cooling may also be significant, as noted by Jeevanjee (2022). This conceptual model has long been used to understand the dynamics of the tropical atmosphere and its vertical structure is well documented in previous work (e.g., Bony et al., 2016; Hartmann & Larson, 2002; Jeevanjee, 2022; Knutson & Manabe, 1995; Zelinka & Hartmann, 2010). Briefly, there is a peak in D_r around the ∼220 K level arising from the rapid decline in radiative cooling with height there. M decreases rapidly with height at this same level, resulting in an upper-level maximum in net detrainment that approximately balances the peak in D_r. The maximum in net detrainment corresponds closely to the level of peak anvil cloud formation.

Previous work has also identified robust responses of this system to surface warming. M is expected to broadly decrease with warming (Held & Soden, 2006; Jeevanjee, 2022; Jenney et al., 2020; Knutson & Manabe, 1995), and the upper-level maximum in D_r is expected to decrease in magnitude (Bony et al., 2016; Saint-Lu et al., 2020) and shift upward to lower pressure such that it maintains roughly the same temperature (Hartmann & Larson, 2002; Zelinka & Hartmann, 2010). If Equation 3 is valid, these changes in D_r would be accompanied by a similar decrease and upward shift in the upper-level $\partial_p M$ maximum. This is the basis of the Fixed Anvil Temperature and Proportionally Higher Anvil Temperature hypotheses, which specify that changes in the temperature of anvil cloud *top* are small compared to changes in surface temperature.

We use this conceptual framework to understand circulation variability throughout the cycle. M is set equal to $-\omega$ for cloudy grid cells and zero elsewhere, then averaged across space and time at each vertical level. Grid cells are considered cloudy if the total condensed water mixing ratio exceeds 10^{-5} kg/kg; precipitating condensate is included here to avoid discontinuities arising from the fact that the microphysics scheme distinguishes between precipitating and nonprecipitating condensate for liquid but not for ice. Note that M defined in this manner retains units of pressure velocity (hPa/day) rather than a true mass flux (kg/m^2/s); the difference between the two is the gravitational acceleration constant g which has no qualitative impact on results.

We first examine variability in M by finding the empirical orthogonal functions (EOFs) of the daily mean, 100–850 hPa M profile. The PBL is excluded such that the EOFs reflect free-tropospheric convection. Prior to computing the EOFs, M is low-pass filtered (4th-order Butterworth filter with a 50-day cutoff) to remove high-frequency variability associated with fast gravity wave propagation. The EOFs thus explain variability of free-tropospheric M on timescales similar to that of the internal cycle. The first two EOFs are shown in Figure 9c, and their vertical gradients, which indicate net detrainment, are shown in Figure 9d. The corresponding principal components (PCs) are shown in Figure 9f.

The first EOF accounts for about half of the low-frequency variance in M and represents variability driven by changes in large-scale convective organization. The corresponding PC is highly correlated with σ_{SST} ($r = 0.91$;

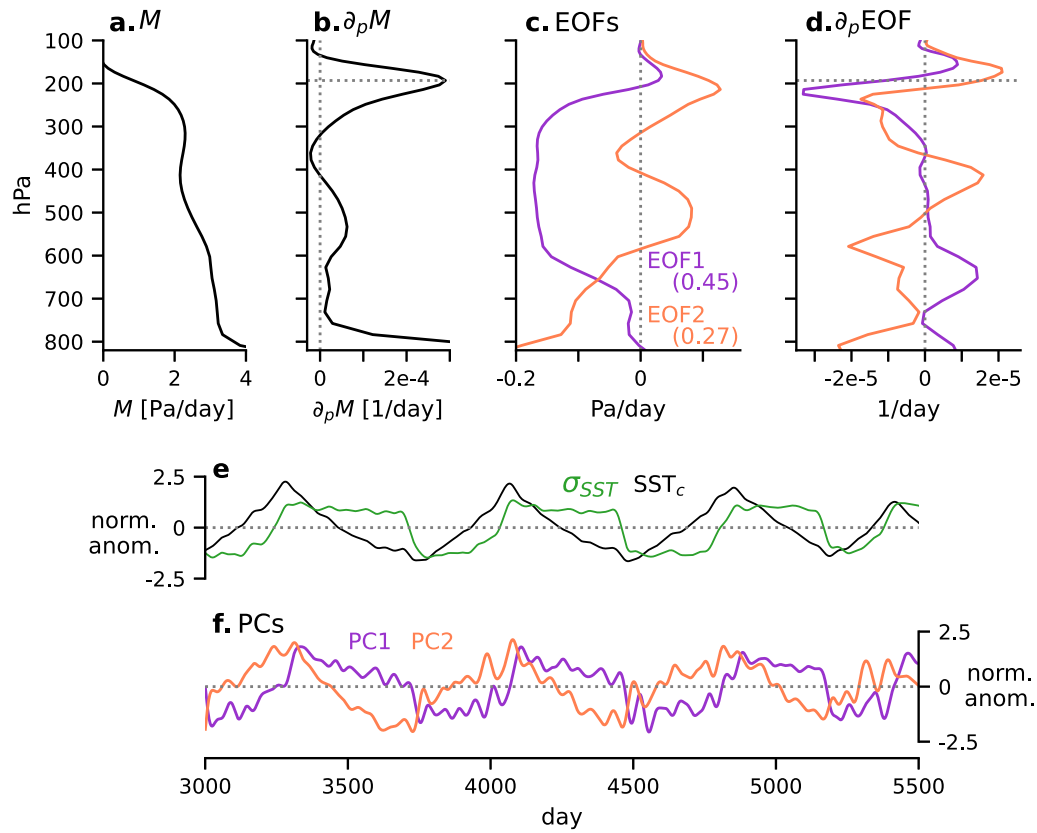

Figure 9. (a) The mean convective mass flux M and (b) net convective detrainment. (c) The first two empirical orthogonal functions (EOFs) of M and (d) their vertical gradient. In panel (c), the numbers in the legend show the fraction of variance explained by each EOF. The horizontal dashed lines in panel (b) and (d)show the level of maximum detrainment. (e) Time series of the normalized anomalies of SST_c and σ_{SST}. (f) The first two principal components corresponding to the EOFs shown in panel (c).

Figure 9f), suggesting that EOF1 represents the sensitivity of M to SST contrast and the number of convective regions present across the domain. When PC1 is positive, EOF1 contributes to reduced mass flux between 250 and 650 hPa and only minor changes in M elsewhere, which implies an increase in net midlevel (600–700 hPa) detrainment at the expense of detrainment aloft (Figure 9d). This shift toward a more bottom-heavy circulation is accompanied by a decrease in anvil cloud area (not shown), as would be expected from reduced upper-level detrainment (Beydoun et al., 2021; Bony et al., 2016; Zelinka & Hartmann, 2010). That the circulation is more bottom-heavy when there is only one convective region is consistent with the finding by Sokol and Hartmann (2022) that greater degrees of convective organization are associated with enhanced midlevel detrainment in idealized RCE simulations.

To understand these organization-driven changes in vertical structure, we turn to the conceptual model described earlier in this section. Figure 10 shows profiles of relevant quantities from the conceptual model averaged over the high- and low-contrast phases of the cycle. The averaging is done such that the mean SST_c during the two averaging periods is roughly equal (within 0.1 K), meaning differences between the two periods result solely from differences in σ_{SST} and large-scale convective organization. To achieve this, we only consider periods when SST_c is between 301.1 and 303.0 K (~70% of the simulation). The resulting profiles of M (Figure 10d) are in line with the expectations from the vertical structure of EOF1 and the variation of PC1 between the phases (Figures 9c and 9f): M is smaller during the high-contrast phase between 250 and 650 hPa and relatively insensitive to SST contrast above and below that layer. This pattern is also seen in profiles of ω_r (Figure 10c), which in equilibrium should roughly balance M. Equation 5 tells us that the reduction in ω_r during the high-contrast phase can arise from an increase in static stability (Figure 10b) or a decrease in radiative cooling (Figure 10a). The dotted line in Figure 10c shows the impact of enhanced stability on ω_r, computed from Equation 5 using the low-contrast Q_r

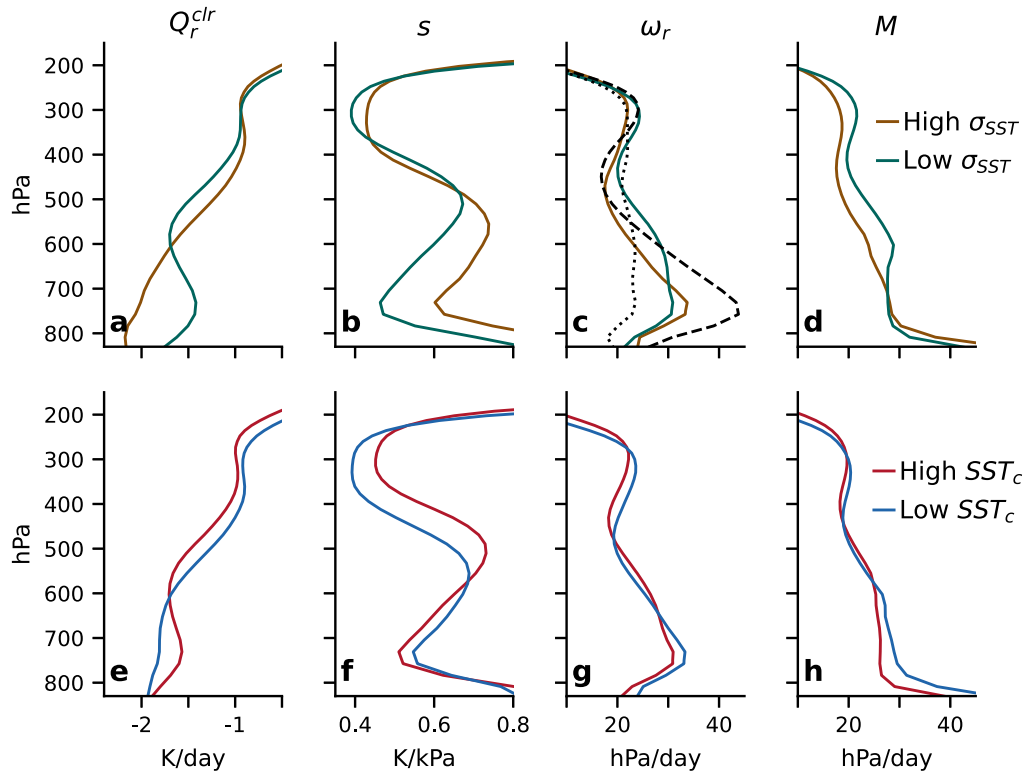

Figure 10. Vertical profiles comparing the (top) high-σ_{SST} and low-σ_{SST} phases and (bottom) high-SST_c and low-SST_c parts of the cycle. (a), (e) Clear-sky radiative cooling rate, (b), (f) static stability, (c), (g), radiatively driven subsidence, and (d), (h) convective mass flux. In panel (c), the dotted black line shows ω_r computed using Q_r from the low-σ_{SST} phase and s from the high-σ_{SST} phase; vice versa for the dashed black line.

profile and the high-contrast s profile. The increase in 500–850 hPa s during the high-contrast phase acts to slow the circulation throughout all the troposphere, with the exception of a narrow layer between 350 and 450 hPa in which circulation strength is minimally affected. The reduction in ω_r is largest at lower levels, meaning the change in stability s acts to reduce the bottom-heaviness of the circulation. The dashed line in Figure 10c shows the impact of changes in the radiative cooling profile on ω_r, computed using the high-contrast Q_r profile and the low-contrast s profile. Changes in the Q_r profile during the high-contrast phase make the circulation more bottom-heavy by strengthening low-level ω_r and weakening mid-level ω_r. These changes result from a shift in radiative cooling to lower levels during the high-contrast phase (Figure 10a), which is a known impact of convective organization (Emanuel et al., 2014). Thus, during the high-contrast phase, changes in stability act to slow the circulation while changes in Q_r affect its vertical structure. The notable, ∼20% increase in mid- and low-level stability during the high-σ_{SST} phase will be explored in the next section.

The second EOF of M accounts for 27% of its low-frequency variance. PC2 is well correlated with SST_c ($r = 0.85$), suggesting that EOF2 represents temperature-driven variability, that is, the impact of absolute SST on the convective mass flux. The vertical structure of EOF2 (Figure 9c) contains two important features. First, as PC2 increases during periods of SST warming, the mass flux profile M shifts upward to lower pressure. This upward shift is well documented in previous work (Hartmann & Larson, 2002; Saint-Lu et al., 2020; Zelinka & Hartmann, 2010). Here, the shift is evident in the vertical gradient of EOF2 (Figure 9d), which represents net detrainment and has two dipoles centered at 210 and 500 hPa. These levels coincide with the mid- and upper-level maxima in the mean detrainment profile (Figure 9b), indicative of an upward shift. The shift can also be seen in Figures 10e–10h, in which the high-SST_c and low-SST_c averages each reflect 30% of the total simulation time and include equal time from the high- and low-contrast phases of the cycle. The second important feature of EOF2 is the general decrease in M between 600 and 850 hPa associated with warmer SST_c, which is also seen in Figure 10h. This, too, is in line with the expected slowdown of the overturning circulation in response to surface warming (Held & Soden, 2006; Jeevanjee, 2022; Knutson & Manabe, 1995). Here, the decrease in M applies only

from 600 to 850 hPa; at higher levels, warmer surface temperatures drive compensating changes in radiative cooling and static stability such that ω_r and M are relatively unaffected. As a result, the profile of M is more bottom-heavy during the cooler parts of the cycle, although the difference in vertical structure is significantly smaller than that associated with changes in σ_{SST} and convective organization.

The EOF analysis shown here provides a convenient separation between σ_{SST}-driven and SST_c-driven circulation variability, which we interpret here as organization- and temperature-driven variability, respectively. The dominant mode of variability is the organization-driven trade-off between the deep and congestus modes of the large-scale overturning circulation. SST_c-driven variability is secondary and acts primarily to shift the profile of M up and down such that it maintains approximately constant temperature. It seems likely that the relative importance of convective organization and temperature is sensitive to their respective amplitudes of variability throughout the internal cycle. For example, if the amplitude of the SST_c cycle were to double but the cycle of convective organization remained the same, SST_c could overtake convective organization as the dominant driver of M variability.

5. Tropospheric Stratification Throughout the Cycle

We now examine how the dry static stability of the free troposphere varies throughout the internal cycle. Stability affects many important tropical phenomena, such as convective intensity and overturning circulation strength (Knutson & Manabe, 1995; Singh & O'Gorman, 2015; Sohn et al., 2016). Here, we are interested in stability because of its role in modulating the mass flux variability discussed in the previous section.

In pressure coordinates, the static stability s is given by

$$s = -\frac{T}{\theta}\frac{\partial \theta}{\partial p} = (\Gamma_d - \Gamma)/\rho g. \tag{6}$$

where Γ is the lapse rate and Γ_d the dry adiabatic lapse rate. Free-tropospheric s is known to be affected by several factors. The first is the thermodynamic state of the sub-cloud layer in the convecting region, which determine the moist adiabatic temperature profile assumed by rising convective updrafts, which is then transmitted by gravity waves across convective and subsiding regions alike (Bretherton & Smolarkiewicz, 1989; Emanuel et al., 1994). Because warmer moist adiabats are more stable, we expect warmer SST_c to be associated with greater s (Bony et al., 2016; Knutson & Manabe, 1995). Second, s is affected by the deviations of rising updrafts from an undiluted moist adiabat. These deviations, which decrease s, arise from the entrainment of dry air into convective updrafts (Bao & Stevens, 2021; Becker & Hohenegger, 2021; Keil et al., 2021; Wing & Singh, 2024). Their magnitude depends on the entrainment rate, ϵ, and the saturation deficit of entrained air. If ϵ is large and/or ambient air is dry, updrafts will follow a less stable temperature profile. When convection is highly organized, updrafts are surrounded by air that is, on average, moister. Therefore, under constant ϵ, increases in convective organization are associated with reduced entrainment cooling, and convective updrafts adhere more closely to an undiluted moist adiabat. Following Becker et al. (2018), we refer to this as the "moist shell" effect, which implies an increase in s with greater convective clustering. Changes in ϵ also impact s, but they will not be our focus here due to the difficulty of estimating ϵ from our simulation output. Finally, vertical gradients in Q_r are thought to affect s, both in the real tropics (Mapes & Zuidema, 1996) and idealized RCE simulations (Sokol & Hartmann, 2022). We diagnose the tendency of s due to radiative heating as $(\partial_t S)_r = -\partial_p Q_r$. While other processes may also affect s in the real world, we will show that the s variability examined here can be largely explained by these factors.

Figures 11a and 11b shows that s variability throughout the cycle has different drivers in different parts of the troposphere. Between the freezing level and ~250 hPa, monthly mean s anomalies closely follow those in SST_c (r^2 = 0.7–0.9, depending on the pressure level; Figure 11b). The association of warmer SST_c with enhanced upper-level stability is consistent with the expectations outlined above: when SST_c is anomalously warm, isotherms shift upward to lower pressure. Since the moist adiabatic lapse rate is primarily a function of temperature, the lapse rate at fixed pressure decreases (s increases) as the surface warms.

On the other hand, between the top of the PBL and the freezing level, monthly mean s is entirely uncorrelated with SST_c (Figure 11b). Rather, variability in s at these levels follows variability in σ_{SST} (r^2 =0.7–0.8). s is large during

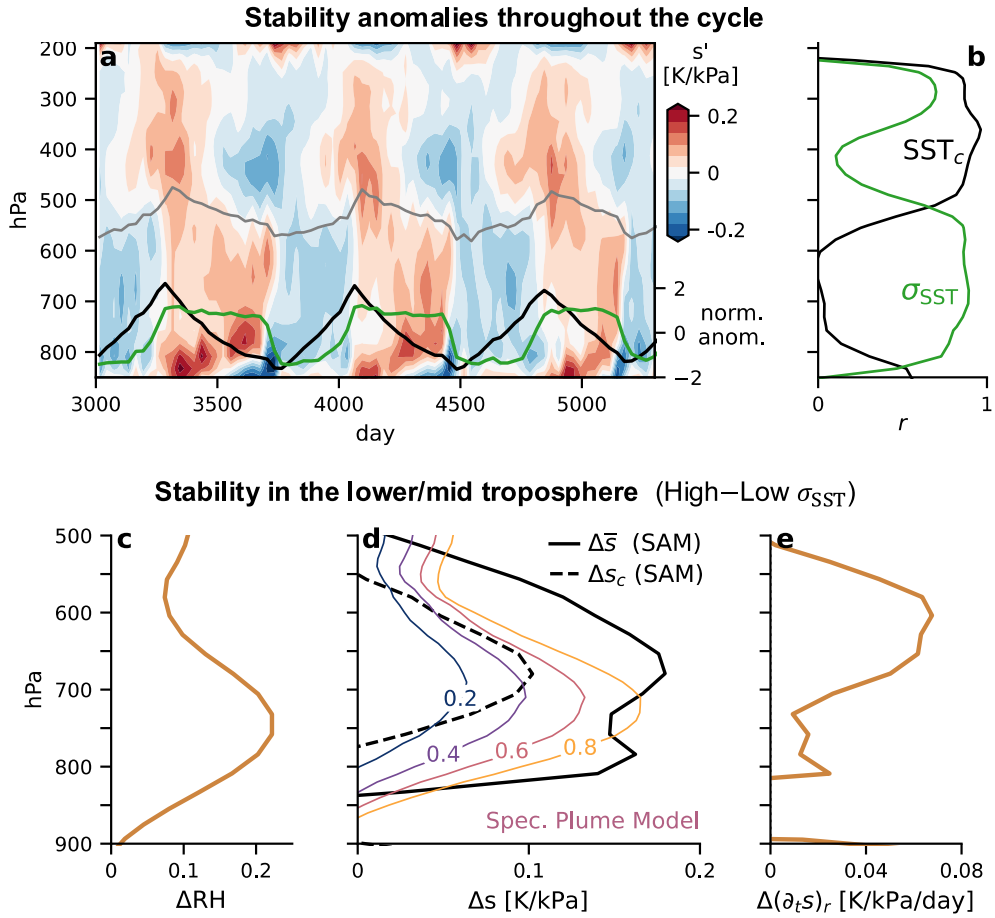

Figure 11. (a) Shading shows monthly s anomalies. The gray line shows the freezing level. Normalized anomalies of SST_c (black) and σ_{SST} (green) are shown on a separate y-axis. (b) Correlation coefficients between monthly mean s and (black) SST_c and (green) σ_{SST}. (c) Difference in convective-region relative humidity between the high- and low-contrast phases. (d) Black: difference in (solid) domain mean and (dashed) convective region s. Colored lines: difference in s predicted by the spectral plume model for various entrainment rates (expressed in km^{-1}.) and a lifting condensation level of 500 m. (e) Difference in domain-averaged $(\partial_t S)_r$. Note the difference in y-axis limits between the top and bottom rows.

the high-contrast phase of the cycle, when there is one convective region, and small during the low-contrast phase, when there are two. This pattern is seemingly consistent with the "moist shell" effect described above, in which greater convective clustering mitigates the effects of entrainment on the temperature profile. In the remainder of this section, we consider whether this explanation can indeed account for this pattern of s variability. For this analysis, we compare two 50-day periods for which the full, vertically resolved model output is available: one high-contrast period (day 7,620–7,670) and one low-contrast period (day 7,800–7,850). The two periods were chosen to have equal SST_c, ensuring that differences in s reflect differences in large-scale convective organization. To identify convective regions, we compute the 50-day, 400–700 hPa mean ω at each grid point then block-average the domain into 162-km blocks. Blocks with mean ascent are defined as the convective regions, and our results are not very sensitive to the details of this procedure.

Figure 11d shows the difference in domain-averaged stability ($\Delta\bar{s}$) and convective-region stability (Δs_c) between the high- and low-contrast periods. Surprisingly, $\Delta\bar{s}$ is significantly larger than Δs_c throughout the 500–800 hPa range. This indicates (a) that the model domain is large enough to support non-negligible horizontal temperature gradients, and (b) that convective processes alone cannot explain the entire relationship between s and σ_{SST}.; the difference between $\Delta\bar{s}$ and Δs_c implies that clear-sky processes have a significant impact on s variability. Above the PBL, the difference between $\Delta\bar{s}$ and Δs_c must arise from changes in radiative cooling between the high- and low-contrast periods. Figure 11e shows that $(\partial_t s)_r$ is greater during the high-contrast period, meaning that changes

in the profile of Q_r act to stabilize the atmosphere. This results from enhanced low-level radiative cooling (Figure 10a) which, as discussed in Section 4, is a known effect of convective organization (Emanuel et al., 2014).

Recognizing that radiative cooling plays a significant role in s variability, we now focus exclusively on Δs_c and consider whether it can be attributed to the moist shell effect. The basis of the moist shell effect is that the ambient air entrained into convective updrafts is more humid when convection is more tightly clustered. Indeed, Figure 11c shows that the mean convective-region RH is significantly greater during the high-contrast phase, with the largest difference of 0.22 found at 750 hPa. To test whether this RH enhancement can explain Δs_c, we employ the spectral plume model (SPM) developed by Zhou and Xie (2019). The SPM can be used to construct the temperature profile resulting from a spectrum of convective plumes with varying entrainment rates and levels of neutral buoyancy. We use the SPM to predict Δs_c resulting from the environmental RH enhancement shown in Figure 11c, assuming negligible differences in ϵ between the high- and low-contrast phases. Our implementation of the SPM takes as inputs a cloud-base entrainment parameter ϵ_0 and a profile of environmental RH, among other parameters, and outputs a profile of s. The full details of our model implementation and experimental protocol can be found in Appendix A. Since the entrainment rate cannot be diagnosed directly from our model output in a straightforward manner, we test a range of reasonable values for ϵ_0 informed by Zhou and Xie (2019) and a recent analysis by Hu et al. (2024), which used the same model and a similar horizontal resolution (4 km rather than our 3 km) as our simulation.

The colored lines in Figure 11d show the SPM-predicted Δs_c for various values of ϵ_0. The SPM-predicted profiles and the SAM-simulated Δs_c (dotted black line) have different shapes throughout the lower troposphere, which is to be expected due to the many simplifying assumptions made by the SPM. Our goal here is simply to determine whether the SPM predicts stability enhancement of the same order of magnitude as that simulated by SAM. Figure 11d shows that values of ϵ_0 between 0.3 and 0.6 km^{-1} produce the best agreement between 550 and 750 hPa. This range of ϵ_0 includes the entrainment rates diagnosed in Hu et al. (2024) for SAM simulations with a similar horizontal resolution. This suggests that the enhancement of RH within convective regions can, under typical entrainment rates, produce an increase in midlevel s that is commensurate with the variations in midlevel s_c throughout the cycle. We therefore find support for the moist shell hypothesis as a plausible mechanism of s variability. This conclusion comes with two important caveats. First, we have assumed constant entrainment rates between the high- and low-contrast phases of the cycle. Second, while RH enhancement likely contributes to $\overline{s}$ variability, clear-sky processes seem equally important.

5.1. Applicability to the Real Tropics

We have found that internal s variability is controlled by different factors at different levels, with a clear split between SST_c-modulated and organization-modulated levels (Figure 11b). As with the circulation variability discussed in Section 4, we suspect that this finding is sensitive to the amplitude of variability in SST_c and convective organization throughout the cycle. Nevertheless, it seems likely that the clear split between SST_c- and organization-modulated levels seen here ultimately reflects two basic, thermodynamic insights. First, the impact of surface temperature variability on the tropospheric temperature profile is amplified aloft. This has long been known and arises from the physics of idealized, moist adiabatic ascent (Manabe & Stouffer, 1980). Second, the importance of the moist shell effect decreases with height; since the impact of dry-air entrainment on the temperature profile is weaker at cold temperatures, the same environmental RH enhancement has less of an effect aloft than at lower, warmer levels.

To understand the applicability of these findings to the real tropics, we examine s variability in the equatorial Pacific in ERA5. We compute monthly mean values of two predictor variables: (a) SST_c, using the same definition as in the model simulation, and (b) var($\mathcal{H}$), the spatial variance of the column RH $\mathcal{H}$, which is a frequently used metric of convective organization (e.g., Wing et al., 2017, 2020). We use var($\mathcal{H}$) instead of σ_{SST} because many factors not present in our simulation can influence real tropical σ_{SST}, which complicates the relationship between σ_{SST} and convective organization. var($\mathcal{H}$), on the other hand, is a more direct measure of convective organization. In the study region of interest (15°S–15°N, 140°–260°E), the principal source of var($\mathcal{H}$) variability is the seasonal migration of the Intertropical Convergence Zone (ITCZ), which produces a var($\mathcal{H}$) maximum in late boreal summer, when the ITCZ is furthest north, and a minimum in late boreal winter, when the ITCZ is furthest south and a secondary convergence zone develops south of the equator. A more detailed picture of this variability can be in found Text S1 and Figure S5 in Supporting Information S1.

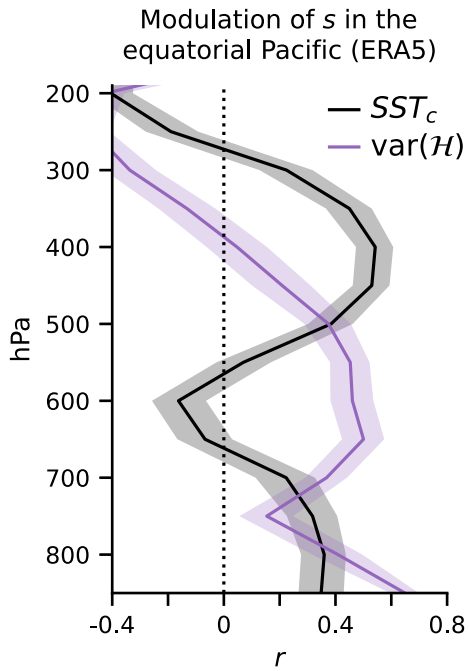

Figure 12. Monthly mean s-SST_c and s-var($\mathcal{H}$) relationships in ERA5 reanalysis. Profiles show correlation coefficients for each variable pair at each level. Shading shows the 95% confidence interval based on 10,000 bootstrapped samples.

Figure 12 shows that the relationships between s and the two predictor variables are generally weaker than in the model simulation, which is to be expected due to the many factors that may influence s in the real tropics that are absent in nonrotating RCE. However, the results are qualitatively similar to the model: the strength of the s-SST_c relationship is strongest in the upper troposphere and weaker at lower levels, while the s-var($\mathcal{H}$) relationship is strongest at and below the freezing level (~550 hPa) and weaker aloft. That the SST_c and organization-modulated levels align so well with the simulation is somewhat surprising given the simplicity of this analysis. Nevertheless, it underscores the fact that the physical mechanisms connecting s, SST_c, and convective organization are rooted in first principles and may therefore apply to the real tropics. While the dependence of upper-level s on surface temperature has been documented in previous work (Saint-Lu et al., 2020), the dependence of midlevel s on convective organization has not, to our knowledge, been examined in any observationally derived data. Because var($\mathcal{H}$) is only one measure of convective organization, and because the tropospheric temperature in the equatorial Pacific is affected by factors not included in our simulation, we caution against a causal interpretation of this result. A closer examination of variability in the vertical structure of RH within convective parts of the tropics would shed more light on these results, but we leave such an analysis for future work.

6. Summary and Discussion

We have examined internal variability in a 21-year, cloud-resolving RCE simulation with a slab ocean. To our knowledge, this is the first description of low-frequency climate variability in a coupled cloud-resolving model. The model produces coherent oscillations of $\overline{SST}$, σ_{SST}, and convective organization that share certain characteristics with previous, idealized GCM experiments (Coppin & Bony, 2017; Drotos et al., 2020; Dygert & Hartmann, 2023) but are nevertheless unique.

The internal oscillation arises because the high- and low-contrast states of the coupled system are both unstable on long timescales. The instability of the high-contrast state arises from the cold edge-warm center SST pattern within the subsiding region, which grows over time until it spawns a new, second, convective region. In the low-contrast state, random perturbations and resulting diabatic feedbacks cause the two convective regions to merge into one, but seemingly only once $\overline{SST}$ is sufficiently warm. *When* these instabilities are triggered is what ultimately sets the amplitude and period of each cycle iteration. And while the cycle amplitude does indeed vary, it is clear that the phase transitions tend to occur within relatively narrow ranges of $\overline{SST}$. The existence of critical temperatures in tropical RCE has been suggested previously for the case of fixed, uniform SSTs (Emanuel et al., 2014), and we have shown here that similar threshold behavior can also occur in the presence of a coupled, slab ocean. Understanding the physical basis for the limits of the internal cycle could provide useful insights into convection-SST interactions in the real tropics, considering that the mean SST in the equatorial Pacific may, in the foreseeable future, approach the maximum $\overline{SST}$ achieved throughout the cycle (302–303 K).

In addition to describing the cycle in detail, we have also examined variability in the convectively coupled overturning circulation and tropospheric stratification. That analysis showed that surface temperature and large-scale convective organization have distinct signatures on the structure of the troposphere and the atmospheric circulation. Convective organization dominates variability in the strength and structure of the overturning circulation, while the modest variations in absolute SST realized throughout the cycle have a more subtle impact. In addition, convective organization has a large influence on mid- and low-level stratification via its impact on low-level radiative cooling and the spatial distribution of moisture. An important takeaway from that analysis is that variability in the profile of radiative cooling has a large impact on free tropospheric stability in RCE. This underscores the limitations of the assumption that the domain-average temperature profile is set by temperature trajectory of convective updrafts. Horizontal temperature gradients can be increasingly sustained as the length of the model domain increases beyond the dissipation lengthscale of gravity waves. At scales similar to that of the

Pacific basin, as shown in Section 5, the spatial contrasts in tropospheric stability are of similar magnitude to its organization-driven variability.

We suspect that many aspects of the internal cycle may be sensitive to experimental design. One potential sensitivity is to the length of the model domain. The domain used here is about equal in length to the equatorial Pacific, and initial sensitivity tests show that the cycle is not substantially affected by modest (up to ∼15%) variations in domain length. However, on even smaller domains, the high-σ_{SST} state becomes stable and the cycle ceases. This appears to be related to a significant weakening of the cold edge-warm center SST pattern in the subsiding region, which underscores the importance of that pattern to the internal cycle discussed here. The scale dependence of tropical RCE circulations, both with and without interactive SSTs, is a rich topic worthy of continued research.

In addition to domain length, horizontal resolution could plausibly affect our results through its impact on low cloud properties (Blossey et al., 2009; Cheng et al., 2010; Radtke et al., 2021). Nudging of the mean flow is another potential sensitivity. In our simulation, the cold edge-warm center SST pattern is amplified by a particular pattern of low cloudiness that is stationary over time due to the fact that the mean flow is nudged to zero. We nudged the wind in this manner so that SSTs could respond to local energy flux perturbations induced by atmospheric features before those features were advected away. Coupled atmosphere-ocean dynamics in the real tropics are affected by both transient and stationary features, and the results shown here highly the need for careful consideration of the balance between realism and idealization in the study of coupled dynamics.

Future work may explore the sensitivity of coupled, internal variability to changes in mean climate. The Q-flux in this experiment was selected such that the resulting SSTs were comparable to the present-day equatorial Pacific, but GCM experiments have shown that several aspects of internal variability are sensitive to changes in mean state brought about by perturbations to CO_2 (Drotos et al., 2020) and insolation (Hartmann & Dygert, 2022). Finally, another question raised by this study is whether the variability generated by CRMs differs meaningfully from that generated by GCMs with parameterized convection. The variability described here is indeed different from previous GCM experiments, but the GCM experiments themselves contain a wide range of results (Coppin & Bony, 2017; Drotos et al., 2020; Dygert & Hartmann, 2023; Popke et al., 2013; Reed et al., 2015). Fully understanding the impacts of resolved convection on coupled variability requires much more than the single simulation discussed here. The potential sensitivities mentioned above provide a starting point for the systematic evaluation of these differences.

Appendix A: Spectral Plume Model Calculations

To understand changes in static stability throughout the cycle, we employ the spectral plume model (SPM) developed by Zhou and Xie (2019) (hereafter ZX19). The SPM builds on the zero-buoyancy plume model developed by Singh and O'Gorman (2013) and can be used to understand the vertical structure of the atmosphere resulting from a spectrum of entraining plumes with different levels of neutral buoyancy. Its equations predict the deviation of the mean moist static energy (h) profile from an undiluted moist adiabat. The formulation used here, copied from ZX19, is

$$\frac{d\Delta h}{dz} - \lambda \Delta h = -\epsilon(z)(1 - RH)\frac{L_v \overline{q_v^*}}{C_p} \tag{A1}$$

$$\lambda \cong \frac{1}{1 + \eta\epsilon(z)(z - z_b)}\frac{d \ln \epsilon}{dz} \tag{A2}$$

where Δh is the deviation of the mean h profile from that of an undiluted moist adiabat, $\overline{q_v^*}$ is the saturation vapor pressure of the entrained environmental air, L_v is the latent heat of vapourization, and C_p is the specific heat capacity of air at constant pressure. η is a constant equal to 0.75, as shown in ZX19. $\epsilon(z)$ is the entrainment rate of a plume reaching its level of neutral buoyancy at height z and is given by

$$\epsilon(z) = \begin{cases} \epsilon_0 \left(\dfrac{z_t - z}{z_t - z_b} \right)^k, & z_b < z < z_t \\ 0, & \text{elsewhere} \end{cases} \tag{A3}$$

where ϵ_0 is the cloud-base entrainment rate, z_t is the top of the convectively mixed layer, here set to 14 km, and z_b is the height of cloud base (i.e., the LCL), which here is 500 m. k is a constant that here, as in ZX19, is set equal to 1.

As shown in ZX19, A1 can be integrated upward to find the vertical profile of Δh. The deviation of the mean temperature profile from the undiluted moist adiabat can then be found by

$$\Delta T(z) = -\left(1 + \frac{L_v}{R_v \overline{T}^2} \frac{L_v \overline{q_v^*}}{C_p} \right)^{-1} \Delta h \tag{A4}$$

where R_v is the gas constant for water vapor and $\overline{T}$ is the environmental temperature profile equal to $T^u + \Delta T$, where T^u is the temperature of the undiluted moist adiabat.

Our version of the SPM takes the following parameters as inputs: the surface temperature, the initial plume RH, ϵ_0, and a vertical profile of environmental RH to use in Equation A1. We select the initial plume RH such that the resulting LCL is 500 m. The plume equation (Equation A1) is then integrated upwards and the resulting profile of environmental $\overline{T}(z)$ is used to compute s.

Our goal is to determine whether the RH enhancement shown in Figure 11c can account for the difference in convective-region s between the low- and high-contrast phases of the cycle. We first run the SPM using inputs from the 50-day, low-contrast sample period. The input RH profile is set to the mean RH within the convective parts of the domain, and a profile of s is generated for each test value of ϵ_0. We then run the model again using the same surface temperature but the RH profile from the high-contrast sample period, which allows us to compute the change in s resulting from RH enhancement within the convecting regions. Results are shown in Figure 11d, with each line corresponding to a different value of ϵ_0.

Data Availability Statement

Code and model output for this paper are available from https://zenodo.org/records/12208410 (Sokol, 2025). The System for Atmospheric Modeling (SAM) is available from http://rossby.msrc.sunysb.edu/SAM.html. ERA5 reanalysis data sets are available from the Copernicus Climate Data Store (Hersbach et al., 2023a, 2023b).

Acknowledgments
We thank Pedro Angulo-Umana, Rob Wood, Kyle Armour, and Chris Bretherton for helpful comments and discussions. We are grateful to Jishi Zhang and one anonymous reviewer for their constructive feedback. This work was supported by NASA FINESST Grant 80NSSC20K1613 and NSF Grants AGS-2124496 and OISE-1743753. We acknowledge high-performance computing support from Cheyenne (10.5065/D6RX99HX) provided by NCAR's Computational and Information Systems Laboratory, sponsored by the National Science Foundation.

References

Andrews, T., Gregory, J. M., Paynter, D., Silvers, L. G., Zhou, C., Mauritsen, T., et al. (2018). Accounting for changing temperature patterns increases historical estimates of climate sensitivity. *Geophysical Research Letters*, *45*(16), 8490–8499. https://doi.org/10.1029/2018GL078887

Back, L. E., & Bretherton, C. S. (2009). On the relationship between SST gradients, boundary layer winds, and convergence over the tropical oceans. *Journal of Climate*, *22*(15), 4182–4196. https://doi.org/10.1175/2009JCLI2392.1

Bao, J., & Stevens, B. (2021). The elements of the thermodynamic structure of the tropical atmosphere. *Journal of the Meteorological Society of Japan. Ser. II*, *99*(6), 1483–1499. https://doi.org/10.2151/jmsj.2021-072

Becker, T., Bretherton, C. S., Hohenegger, C., & Stevens, B. (2018). Estimating bulk entrainment with unaggregated and aggregated convection. *Geophysical Research Letters*, *45*(1), 455–462. https://doi.org/10.1002/2017GL076640

Becker, T., & Hohenegger, C. (2021). Entrainment and its dependency on environmental conditions and convective organization in convection-permitting simulations. *Monthly Weather Review*, *149*(2), 537–550. https://doi.org/10.1175/MWR-D-20-0229.1

Beydoun, H., Caldwell, P. M., Hannah, W. M., & Donahue, A. S. (2021). Dissecting anvil cloud response to sea surface warming. *Geophysical Research Letters*, *48*(15), e2021GL094049. https://doi.org/10.1029/2021GL094049

Bjerknes, J. (1969). Atmospheric teleconnections from the equatorial Pacific. *Monthly Weather Review*, *97*(3), 163–172. https://doi.org/10.1175/1520-0493(1969)097⟨0163:ATFTEP⟩2.3.CO;2

Blossey, P. N., Bretherton, C. S., & Wyant, M. C. (2009). Subtropical low cloud response to a warmer climate in a Superparameterized climate model. Part II: Column modeling with a cloud resolving model. *Journal of Advances in Modeling Earth Systems*, *1*(3). https://doi.org/10.3894/JAMES.2009.1.8

Bony, S., Stevens, B., Coppin, D., Becker, T., Reed, K. A., Voigt, A., & Medeiros, B. (2016). Thermodynamic control of anvil cloud amount. *Proceedings of the National Academy of Sciences*, *113*(32), 8927–8932. https://doi.org/10.1073/pnas.1601472113

Bretherton, C. S., Blossey, P. N., & Khairoutdinov, M. (2005). An energy-balance analysis of deep convective self-aggregation above uniform SST. *Journal of the Atmospheric Sciences*, *62*(12), 4273–4292. https://doi.org/10.1175/JAS3614.1

Bretherton, C. S., & Smolarkiewicz, P. K. (1989). Gravity waves, compensating subsidence and detrainment around cumulus clouds. *Journal of the Atmospheric Sciences*, *46*(6), 740–759. https://doi.org/10.1175/1520-0469(1989)046⟨0740:GWCSAD⟩2.0.CO;2

Chen, Y.-C., & Yu, J.-Y. (2021). Modes of tropical convection and their roles in transporting moisture and moist static energy: Contrast between deep and shallow convection. *Climate Dynamics*, *57*(7–8), 1789–1803. https://doi.org/10.1007/s00382-021-05777-x

Chen, Y.-T., & Wu, C.-M. (2019). The role of interactive SST in the cloud-Resolving simulations of aggregated convection. *Journal of Advances in Modeling Earth Systems*, *11*(10), 3321–3340. https://doi.org/10.1029/2019MS001762

Cheng, A., Xu, K.-M., & Stevens, B. (2010). Effects of resolution on the simulation of boundary-layer clouds and the partition of kinetic energy to subgrid scales. *Journal of Advances in Modeling Earth Systems*, *2*(1). https://doi.org/10.3894/JAMES.2010.2.3

Coppin, D., & Bony, S. (2017). Internal variability in a coupled general circulation model in radiative-convective equilibrium. *Geophysical Research Letters*, *44*(10), 5142–5149. https://doi.org/10.1002/2017GL073658

Cronin, T. W., & Wing, A. A. (2017). Clouds, circulation, and climate sensitivity in a radiative-convective equilibrium channel model. *Journal of Advances in Modeling Earth Systems*, *9*(8), 2883–2905. https://doi.org/10.1002/2017MS001111

Deser, C., Alexander, M. A., Xie, S.-P., & Phillips, A. S. (2010). Sea surface temperature variability: Patterns and mechanisms. *Annual Review of Marine Science*, *2*(2), 115–143. https://doi.org/10.1146/annurev-marine-120408-151453

Drotos, G., Becker, T., Mauritsen, T., & Stevens, B. (2020). Global variability in radiative-convective equilibrium with a slab ocean under a wide range of CO2 concentrations. *Tellus A: Dynamic Meteorology and Oceanography*, *72*(1), 1–19. https://doi.org/10.1080/16000870.2019.1699387

Dygert, B. D., & Hartmann, D. L. (2023). The cycle of large-scale aggregation in tropical radiative-convective equilibrium. *Journal of Geophysical Research: Atmospheres*, *128*(7), e2022JD037302. https://doi.org/10.1029/2022JD037302

Emanuel, K., Neelin, J. D., & Bretherton, C. S. (1994). On large-scale circulations in convecting atmospheres. *Quarterly Journal of the Royal Meteorological Society*, *120*(519), 1111–1143. https://doi.org/10.1002/qj.49712051902

Emanuel, K., Wing, A. A., & Vincent, E. M. (2014). Radiative-convective instability. *Journal of Advances in Modeling Earth Systems*, *6*(1), 75–90. https://doi.org/10.1002/2013MS000270

Fueglistaler, S. (2019). Observational evidence for two modes of coupling between sea surface temperatures, tropospheric temperature profile, and shortwave cloud radiative effect in the tropics. *Geophysical Research Letters*, *46*(16), 9890–9898. https://doi.org/10.1029/2019GL083990

Grabowski, W. W., Wu, X., Moncrieff, M. W., & Hall, W. D. (1998). Cloud-resolving modeling of cloud systems during Phase III of GATE. Part II: Effects of resolution and the third spatial dimension. *Journal of the Atmospheric Sciences*, *55*(21), 3264–3282. https://doi.org/10.1175/1520-0469(1998)055<3264:crmocs>2.0.co;2

Harrop, B. E., & Hartmann, D. L. (2012). Testing the role of radiation in determining tropical cloud-top temperature. *Journal of Climate*, *25*(17), 5731–5747. https://doi.org/10.1175/JCLI-D-11-00445.1

Hartmann, D. L., & Dygert, B. D. (2022). Global radiative convective equilibrium with a slab ocean: SST contrast, sensitivity and circulation. *Journal of Geophysical Research: Atmospheres*, *127*(12), e2021JD036400. https://doi.org/10.1029/2021JD036400

Hartmann, D. L., & Larson, K. (2002). An important constraint on tropical cloud - Climate feedback. *Geophysical Research Letters*, *29*(20). https://doi.org/10.1029/2002GL015835

Held, I. M., Hemler, R. S., & Ramaswamy, V. (1993). Radiative-convective equilibrium with explicit two-dimensional moist convection. *Journal of the Atmospheric Sciences*, *50*(23), 3909–3927. https://doi.org/10.1175/1520-0469(1993)050⟨3909:RCEWET⟩2.0.CO;2

Held, I. M., & Soden, B. J. (2006). Robust responses of the hydrological cycle to global warming. *Journal of Climate*, *19*(21), 5686–5699. https://doi.org/10.1175/JCLI3990.1

Hersbach, H., Bell, B., Berrisford, P., Biavati, G., Horányi, A., Muñoz-Sabater, J., et al. (2023a). ERA5 monthly averaged data on pressure levels from 1940 to present. *Copernicus Climate Change Service (C3S) Climate Data Store (CDS)*. https://doi.org/10.24381/cds.adbb2d47

Hersbach, H., Bell, B., Berrisford, P., Biavati, G., Horányi, A., Muñoz-Sabater, J., et al. (2023b). ERA5 monthly averaged data on single levels from 1940 to present. *Copernicus Climate Change Service (C3S) Climate Data Store (CDS)*. https://doi.org/10.24381/cds.f17050d7

Hersbach, H., Bell, B., Berrisford, P., Hirahara, S., Horányi, A., Muñoz-Sabater, J., et al. (2020). The ERA5 global reanalysis. *Quarterly Journal of the Royal Meteorological Society*, *146*(730), 1999–2049. https://doi.org/10.1002/qj.3803

Hohenegger, C., & Stevens, B. (2016). Coupled radiative convective equilibrium simulations with explicit and parameterized convection. *Journal of Advances in Modeling Earth Systems*, *8*(3), 1468–1482. https://doi.org/10.1002/2016MS000666

Hu, Z., Jeevanjee, N., & Kuang, Z. (2024). A refined zero-buoyancy plume model for large-scale atmospheric profiles and anvil clouds in radiative-convective equilibrium. *Journal of Advances in Modeling Earth Systems*, *16*(11), e2023MS004050. https://doi.org/10.1029/2023MS004050

Jakob, C., Singh, M. S., & Jungandreas, L. (2019). Radiative convective equilibrium and organized convection: An observational perspective. *Journal of Geophysical Research: Atmospheres*, *124*(10), 5418–5430. https://doi.org/10.1029/2018JD030092

Jeevanjee, N. (2022). Three rules for the decrease of tropical convection with global warming. *Journal of Advances in Modeling Earth Systems*, *14*(11), e2022MS003285. https://doi.org/10.1029/2022MS003285

Jenney, A. M., Randall, D. A., & Branson, M. D. (2020). Understanding the response of tropical ascent to warming using an energy balance framework. *Journal of Advances in Modeling Earth Systems*, *12*(6), e2020MS002056. https://doi.org/10.1029/2020MS002056

Keil, P., Schmidt, H., Stevens, B., & Bao, J. (2021). Variations of tropical lapse rates in climate models and their implications for upper-tropospheric warming. *Journal of Climate*, *34*(24), 9747–9761. https://doi.org/10.1175/JCLI-D-21-0196.1

Khairoutdinov, M. F., & Randall, D. A. (2003). Cloud resolving modeling of the ARM summer 1997 IOP: Model formulation, results, uncertainties, and sensitivities. *Journal of the Atmospheric Sciences*, *60*(4), 607–625. https://doi.org/10.1175/1520-0469(2003)060⟨0607:CRMOTA⟩2.0.CO;2

Knutson, T. R., & Manabe, S. (1995). Time-mean response over the Tropical Pacific to increased C02 in a coupled ocean-atmosphere model. *Journal of Climate*, *8*(9), 2181–2199. https://doi.org/10.1175/1520-0442(1995)008⟨2181:TMROTT⟩2.0.CO;2

Lindzen, R. S., & Nigam, S. (1987). On the role of sea surface temperature gradients in forcing low-level winds and convergence in the tropics. *Journal of the Atmospheric Sciences*, *44*(17). https://doi.org/10.1175/1520-0469(1987)044⟨2418:otross⟩2.0.co;2

Ma, J., Xie, S.-P., & Kosaka, Y. (2012). Mechanisms for tropical tropospheric circulation change in response to global warming. *Journal of Climate*, *25*(8), 2979–2994. https://doi.org/10.1175/JCLI-D-11-00048.1

Manabe, S., & Stouffer, R. J. (1980). Sensitivity of a global climate model to an increase of CO2 concentration in the atmosphere. *Journal of Geophysical Research*, *85*(C10), 5529–5554. https://doi.org/10.1029/JC085iC10p05529

Manabe, S., & Wetherald, R. T. (1967). Thermal equilibrium of the atmosphere with a given distribution of relative humidity. *Journal of the Atmospheric Sciences*, *24*(3), 241–259. https://doi.org/10.1175/1520-0469(1967)024⟨0241:TEOTAW⟩2.0.CO;2

Mapes, B. E., & Zuidema, P. (1996). Radiative-dynamical consequences of dry tongues in the tropical troposphere. *Journal of the Atmospheric Sciences*, *53*(4), 620–638. https://doi.org/10.1175/1520-0469(1996)053⟨0620:RDCODT⟩2.0.CO;2

Morrison, H., Milbrandt, J. A., Bryan, G. H., Ikeda, K., Tessendorf, S. A., & Thompson, G. (2015). Parameterization of cloud microphysics based on the prediction of bulk ice Particle properties. Part II: Case study comparisons with observations and other schemes. *Journal of the Atmospheric Sciences*, *72*(1), 312–339. https://doi.org/10.1175/JAS-D-14-0066.1

Pendergrass, A. G. (2020). Changing degree of convective organization as a mechanism for dynamic changes in extreme precipitation. *Current Climate Change Reports*, *6*(2), 47–54. https://doi.org/10.1007/s40641-020-00157-9

Petch, J. C., Blossey, P. N., & Bretherton, C. s. (2008). Differences in the lower troposphere in two- and three-dimensional cloud-resolving model simulations of deep convection. *Quarterly Journal of the Royal Meteorological Society*, *134*(636), 1941–1946. https://doi.org/10.1002/qj.315

Popke, D., Stevens, B., & Voigt, A. (2013). Climate and climate change in a radiative-convective equilibrium version of ECHAM6. *Journal of Advances in Modeling Earth Systems*, *5*(1), 1–14. https://doi.org/10.1029/2012MS000191

Radtke, J., Mauritsen, T., & Hohenegger, C. (2021). Shallow cumulus cloud feedback in large eddy simulations – Bridging the gap to storm-resolving models. *Atmospheric Chemistry and Physics*, *21*(5), 3275–3288. https://doi.org/10.5194/acp-21-3275-2021

Ramanathan, V., & Collins, W. (1991). Thermodynamic regulation of ocean warming by cirrus clouds deduced from observations of the 1987 El Niño. *Nature*, *351*(6321), 27–32. https://doi.org/10.1038/351027a0

Ramaswamy, V., & Kiehl, J. T. (1985). Sensitivities of the radiative forcing due to large loadings of smoke and dust aerosols. *Journal of Geophysical Research*, *90*(D3), 5597–5613. https://doi.org/10.1029/JD090iD03p05597

Reed, K. A., Medeiros, B., Bacmeister, J. T., & Lauritzen, P. H. (2015). Global radiative–convective equilibrium in the community atmosphere model, version 5. *Journal of the Atmospheric Sciences*, *72*(5), 2183–2197. https://doi.org/10.1175/JAS-D-14-0268.1

Romps, D. M. (2011). Response of tropical precipitation to global warming. *Journal of the Atmospheric Sciences*, *68*(1), 123–138. https://doi.org/10.1175/2010JAS3542.1

Saint-Lu, M., Bony, S., & Dufresne, J.-L. (2020). Observational evidence for a stability Iris effect in the tropics. *Geophysical Research Letters*, *47*(14). https://doi.org/10.1029/2020GL089059

Seeley, J. T., Jeevanjee, N., & Romps, D. M. (2019). FAT or FiTT: Are anvil clouds or the tropopause temperature invariant? *Geophysical Research Letters*, *46*(3), 1842–1850. https://doi.org/10.1029/2018GL080096

Seidel, S. D., & Yang, D. (2022). Temperatures of anvil clouds and radiative tropopause in a wide array of cloud-resolving simulations. *Journal of Climate*, *35*(24), 4465–4478. https://doi.org/10.1175/JCLI-D-21-0962.1

Shamekh, S., Muller, C., Duvel, J.-P., & D'Andrea, F. (2020). How do ocean warm anomalies favor the aggregation of deep convective clouds? *Journal of the Atmospheric Sciences*, *77*(11), 3733–3745. https://doi.org/10.1175/JAS-D-18-0369.1

Singh, M. S., & O'Gorman, P. A. (2013). Influence of entrainment on the thermal stratification in simulations of radiative-convective equilibrium. *Geophysical Research Letters*, *40*(16), 4398–4403. https://doi.org/10.1002/grl.50796

Singh, M. S., & O'Gorman, P. A. (2015). Increases in moist-convective updraught velocities with warming in radiative-convective equilibrium. *Quarterly Journal of the Royal Meteorological Society*, *141*(692), 2828–2838. https://doi.org/10.1002/qj.2567

Sohn, B.-J., Lee, S., Chung, E.-S., & Song, H.-J. (2016). The role of the dry static stability for the recent change in the Pacific Walker circulation. *Journal of Climate*, *29*(8), 2765–2779. https://doi.org/10.1175/JCLI-D-15-0374.1

Sokol, A. B. (2025). Code and model output to accompany "Internal ocean-atmosphere variability in kilometer-scale radiative-convective equilibrium" by Sokol et al. (2025). *Zenodo*. https://doi.org/10.5281/zenodo.12208410

Sokol, A. B., & Hartmann, D. L. (2022). Congestus mode invigoration by convective aggregation in simulations of radiative-convective equilibrium. *Journal of Advances in Modeling Earth Systems*, *14*(7). https://doi.org/10.1029/2022MS003045

Tompkins, A. M. (2000). The impact of dimensionality on long-term cloud-resolving model simulations. *Monthly Weather Review*, *128*(5), 1521–1535. https://doi.org/10.1175/1520-0493(2000)128⟨1521:TIODOL⟩2.0.CO;2

Tompkins, A. M., & Semie, A. G. (2021). Impact of a mixed ocean layer and the diurnal cycle on convective aggregation. *Journal of Advances in Modeling Earth Systems*, *13*(12), e2020MS002186. https://doi.org/10.1029/2020MS002186

Vecchi, G. A., & Soden, B. J. (2007). Global warming and the weakening of the tropical circulation. *Journal of Climate*, *20*(17), 4316–4340. https://doi.org/10.1175/JCLI4258.1

Voigt, A., Albern, N., & Papavasileiou, G. (2019). The atmospheric pathway of the cloud-radiative impact on the circulation response to global warming: Important and uncertain. *Journal of Climate*, *32*(10), 3051–3067. https://doi.org/10.1175/JCLI-D-18-0810.1

Wills, R. C. J., Dong, Y., Proistosecu, C., Armour, K. C., & Battisti, D. S. (2022). Systematic climate model biases in the large-scale patterns of recent sea-surface temperature and sea-level pressure change. *Geophysical Research Letters*, *49*(17), e2022GL100011. https://doi.org/10.1029/2022GL100011

Wing, A. A., Emanuel, K., Holloway, C. E., & Muller, C. (2017). Convective self-aggregation in numerical simulations: A review. *Surveys in Geophysics*, *38*(6), 1173–1197. https://doi.org/10.1007/s1071201794084

Wing, A. A., Reed, K. A., Satoh, M., Stevens, B., Bony, S., & Ohno, T. (2018). Radiative–convective equilibrium model intercomparison project. *Geoscientific Model Development*, *11*(2), 793–813. https://doi.org/10.5194/gmd-11-793-2018

Wing, A. A., & Singh, M. S. (2024). Control of stability and relative humidity in the radiative-convective equilibrium model intercomparison project. *Journal of Advances in Modeling Earth Systems*, *16*(1), e2023MS003914. https://doi.org/10.1029/2023MS003914

Wing, A. A., Stauffer, C. L., Becker, T., Reed, K. A., Ahn, M.-S., Arnold, N. P., et al. (2020). Clouds and convective self-aggregation in a multimodel ensemble of radiative-convective equilibrium simulations. *Journal of Advances in Modeling Earth Systems*, *12*(9), e2020MS002138. https://doi.org/10.1029/2020MS002138

Yamaguchi, T., Randall, D. A., & Khairoutdinov, M. F. (2011). Cloud modeling tests of the ULTIMATE–MACHO scalar advection scheme. *Monthly Weather Review*, *139*(10), 3248–3264. https://doi.org/10.1175/MWR-D-10-05044.1

Zelinka, M. D., & Hartmann, D. L. (2010). Why is longwave cloud feedback positive? *Journal of Geophysical Research*, *115*(16). https://doi.org/10.1029/2010JD013817

Zhou, W., & Xie, S.-P. (2019). A conceptual spectral plume model for understanding tropical temperature profile and convective updraft velocities. *Journal of the Atmospheric Sciences*, *76*(9), 2801–2814. https://doi.org/10.1175/JAS-D-18-0330.1